

# Kilohertz Gravitational Waves from Binary Neutron Star Mergers: Full Spectrum Analyses and High-density Constraints on Neutron Star Matter

Giulia Huez<sup>1</sup>, Sebastiano Bernuzzi<sup>1</sup>, Matteo Breschi<sup>1</sup>, and Rossella Gamba<sup>2,3</sup>

<sup>1</sup>*Theoretisch-Physikalisches Institut, Friedrich-Schiller-Universität Jena, 07743, Jena, Germany*

<sup>2</sup>*Institute for Gravitation and the Cosmos, The Pennsylvania State University, University Park, PA 16802, USA*

<sup>3</sup>*Department of Physics, University of California, Berkeley, CA 94720, USA*

(Dated: July 10, 2025)

We demonstrate Bayesian analyses of the complete gravitational-wave spectrum of binary neutron star mergers events with the next-generation detector Einstein Telescope. Our mock analyses are performed for 20 different signals using the `TEOBResumSPA_NRPMw` waveform that models gravitational-waves from the inspiral to the postmerger phase. They are employed to validate a pipeline for neutron star's extreme matter constraints with prospective detections and under minimal hypotheses on the equation of state. The proposed analysis stack delivers inferences for the mass-radius curve, the mass dependence of the quadrupolar tidal polarizability parameter, the neutron star's maximum density, the maximum mass and the relative radius, and the pressure-density relation itself. We show that a single event at a signal-to-noise ratio close to the minimum threshold for postmerger detection is sufficient to tightly constrain all the above relations as well as quantities like the maximum mass (maximum density) to precision of  $\sim 6\%$  ( $\sim 10\%$ ) at 90% credibility level. We also revisit inferences of prompt black hole formation with full spectrum signals and find that the latter can be robustly identified, even when the postmerger is not detectable due to a low signal-to-noise ratio. New results on the impact of the initial signal frequency and of the detector configuration (triangular vs. two-L) on the source's parameters estimation are also reported. An improvement of approximately one order of magnitude in the precision of the chirp mass and mass ratio can be achieved by lowering the initial frequency from 20 Hz to 2 Hz. The two-L configuration shows instead significant improvements on the inference of the source declination, due to geographical separation of the two detectors.

## I. INTRODUCTION

Binary neutron stars (BNSs) are the main sources for next-generation (XG) ground-based gravitational wave (GW) detectors, such as Einstein Telescope (ET) [1–5] and Cosmic Explorer (CE) [6, 7]. They are expected to be observed with a rate of  $7 \times 10^4$  mergers per year [8–10]. ET is designed with a xylophone configuration, combining a cryogenic interferometer for the low-frequency band with a high-power interferometer targeting frequencies above  $\sim 100$  Hz. This design will not only significantly enhance current GW detector sensitivity, but also enable the observations of postmerger (PM) signals at kilohertz frequencies. GWs observations of the full spectrum (inspiral-merger-postmerger) of a BNS merger can convey unique information on the nuclear matter that constitutes this compact object *e.g.* [11–16], thus improving current GW constraints after GW170817 [17–19]. While the inspiral-merger (IM) carries the footprint of the matter properties at the progenitor densities, *i.e.*  $\rho \lesssim 2\rho_{\text{sat}}$  (where  $\rho_{\text{sat}} \simeq 2.7 \times 10^{14}$  g cm<sup>-3</sup> is the nuclear saturation density), the kilohertz PM transient encodes information about the high-density ( $\sim 3\text{--}6\rho_{\text{sat}}$ ) regime of the equation of state (EoS) [15], enabling the investigation of unrevealed properties of the nuclear matter at high-densities, unreachable with modern experiments [15, 20–23].

Inference of source properties and constraints on the neutron star (NS) EoS requires the availability of complete waveform templates for matched-filtering analyses. These templates are crucially designed using empirical relations computed from numerical relativity (NR) sim-

ulations and connecting morphological features of the PM signal to NS properties, *e.g.* [15, 24–32]. In particular, Breschi *et al.* [13] proposed the first time-domain full spectrum model that was constructed by combining an effective-one-body (EOB) IM waveform with a NR-informed analytical PM model (see also [32, 33]). Similar approaches have been used in [16, 34], where phenomenological frequency-domain IM waveforms are stitched to PM models based on wavelets or Lorentzian templates. In all cases the phenomenological PM parameters are connected to the source parameter using NR empirical relations; see also [35–38] for other examples of analytical PM models and [39, 40] for data-driven PM models, which have not been incorporated in full spectrum models yet.

These modeling efforts, combined with the exceptional sensitivity of XG detectors, provide a crucial foundation for accurate EoS inference. Notably, even a single detection of BNS with ET may suffice to place stringent constraints on the NS mass-radius relation [15]. That approach enabled tight constraints of the mass-radius diagram and demonstrated that the maximum NS mass can be determined with an accuracy better than 12%. Additional works [38, 41–44] have similarly combined information from the IM section to PM features, highlighting the complementarity of these two regimes in probing supranuclear matter. Numerous proof of principle studies focus exclusively on the PM GW emission from BNSs to investigate the high-density nuclear matter through NR simulations. These works exploit the connection between peak frequencies and EoS-dependent properties, such as total mass and compactness [22, 35, 45–50]. Fur-

thermore, recent works explored the potential for EoS inference using advanced and XG detectors [51–55] and assess the impact of different waveform models on nuclear EoS inference [56].

In the cases where the presence of the PM is not detectable, a major issue is the inference of prompt (rapid) black hole (BH) formation after merger. While electromagnetic counterparts can provide valuable information in this regard [18, 57–62], GWs remain the key messenger to identify unambiguously the presence of a remnant BH. Many authors have explored the conditions under which a prompt collapse (PC) occurs instead of the formation of a NS remnant. This is primarily connected to the total mass of the BNS and the EoS of dense nuclear matter [63–67]. In addition, PC analysis can be employed to place constraints on the EoS [12, 66, 68, 69]. Agathos *et al.* [70] presented the first comprehensive Bayesian analysis to assess the probability of PC directly from the inspiral GW signal. This methodology was subsequently applied in the analysis of GW190425 [71].

In this paper, we perform an extensive investigation of the capabilities of ET to infer BNS properties. We firstly focus on the low-frequency regime, assessing the impact on source parameter estimation of the initial frequency and of detector configurations (two-L and triangular). We then concentrate in the detections of the complete GW spectrum and study the prospective accuracy of EoS inference. We develop and employ a full spectrum model which combines the fast frequency-domain EOB `TEOBResumSPA` [72–74] with the frequency-domain wavelet-based `NRPMw` model [32, 33] (Paper I and Paper II hereafter). We then perform Bayesian mock analyses of 20 fiducial BNSs, covering the frequency range from  $f_0 = 20$  Hz up to the kiloHertz regime. These analyses serve not only to demonstrate the feasibility of combining information across the full GW spectrum, from inspiral to merger and postmerger, but also to quantify the achievable accuracy in the inference of source parameters. Beyond parameter estimation, our primary objective is to assess the improvements in constraints on the supranuclear properties governing NS matter. By incorporating both low- and high-frequency components of the signal, we explore how analyses of ET signals enhance our ability to probe the dense-matter regime, including tighter bounds on the mass-radius relation, the maximum mass supported by a stable non-rotating NS and the PC inference.

The paper is structured as follows. In Sec. II we introduce the full spectrum waveform model and the framework used for the analyses. We present the results in Sec. III, covering both inspiral only and full spectrum analyses, as well as a discussion about the EoS constraints and the probability of prompt BH formation. Finally Sec. IV provides a summary and our main conclusion. Moreover, we include Appendices about the waveform model and Bayesian analysis.

*Conventions* – All quantities are expressed in SI units, with masses in Solar masses  $M_\odot$  and distances in

Mpc. The symbol ‘log’ denotes the natural logarithm. The waveform strain is decomposed in multipoles  $(\ell, m)$  as

$$h_+ - ih_\times = D_L^{-1} \sum_{\ell=2}^{\infty} \sum_{m=-\ell}^{\ell} h_{\ell m}(t) {}_{-2}Y_{\ell m}(\iota, \varphi), \quad (1)$$

where  $D_L$  is the luminosity distance,  ${}_{-2}Y_{\ell m}$  are the  $s = -2$  spin-weighted spherical harmonics and  $\iota, \varphi$  are respectively the polar and azimuthal angles that define the orientation of the binary with respect to the observer. Each waveform mode  $h_{\ell m}(t)$  is decomposed in amplitude  $A_{\ell m}(t)$  and phase  $\phi_{\ell m}(t)$ , as

$$h_{\ell m}(t) = A_{\ell m}(t) e^{-i\phi_{\ell m}(t)}, \quad (2)$$

with a related GW frequency,

$$\omega_{\ell m}(t) = 2\pi f_{\ell m}(t) = \frac{d}{dt} \phi_{\ell m}(t). \quad (3)$$

The moment of merger is defined as the time of the peak of  $A_{22}(t)$ . When the  $(\ell, m)$  indices are omitted, we consider only the dominant  $(2, 2)$  mode.

The waveform depends on intrinsic and extrinsic source parameters. The intrinsic parameters of a BNS system are masses, spins and tidal polarizability parameters, *e.g.*  $\theta_{\text{bin}} = \{M, q, \chi_1, \chi_2, \Lambda_1, \Lambda_2\}$ . The total binary mass is indicated with  $M = m_1 + m_2$ , the mass ratio is  $q = m_1/m_2 \geq 1$ , and the symmetric mass ratio is  $\nu = m_1 m_2 / M^2$ . The dimensionless spin vectors are denoted with  $\chi_i$  for  $i = 1, 2$  and the spin component aligned with the orbital angular momentum  $\mathbf{L}$  are labeled as  $\chi_i = \chi_i \cdot \mathbf{L} / |\mathbf{L}|$ . The effective spin parameter  $\chi_{\text{eff}}$  is a mass-weighted, aligned spin combination, *i.e.*

$$\chi_{\text{eff}} = \frac{m_1 \chi_1 + m_2 \chi_2}{M}. \quad (4)$$

The quadrupolar tidal polarizability parameters are defined as  $\Lambda_i = (2/3) k_{2,i} C_i^{-5}$  for  $i = 1, 2$ , where  $k_{2,i}$  and  $C_i$  are the second Love number and the compactness of the  $i$ -th object, respectively. The reduced tidal parameter  $\tilde{\Lambda}$  is

$$\tilde{\Lambda} = \frac{16}{13} \left[ \frac{(m_1 + 12m_2)m_1^4 \Lambda_1}{M^5} + (1 \leftrightarrow 2) \right]. \quad (5)$$

The quadrupolar tidal polarizability  $\kappa_2^{\text{T}}$  is

$$\kappa_2^{\text{T}} = 3\nu \left[ \left( \frac{m_1}{M} \right)^3 \Lambda_1 + (1 \leftrightarrow 2) \right]. \quad (6)$$

The extrinsic parameters of the source  $\theta_{\text{ext}} = \{D_L, \iota, \alpha, \delta, \psi, t_{\text{mrg}}, \phi_{\text{mrg}}\}$ , *i.e.* inclination angle  $\iota$ , right ascension angle  $\alpha$ , declination angle  $\delta$ , polarization angle  $\psi$ , time of coalescence  $t_{\text{mrg}}$ , and phase at the merger  $\phi_{\text{mrg}}$ , allow us to identify the location and orientation of the source. Moreover, we include the recalibration parameters  $\delta_{\text{fit}}$  that account for deviations from the predictions of the EoS-insensitive relations consistently with

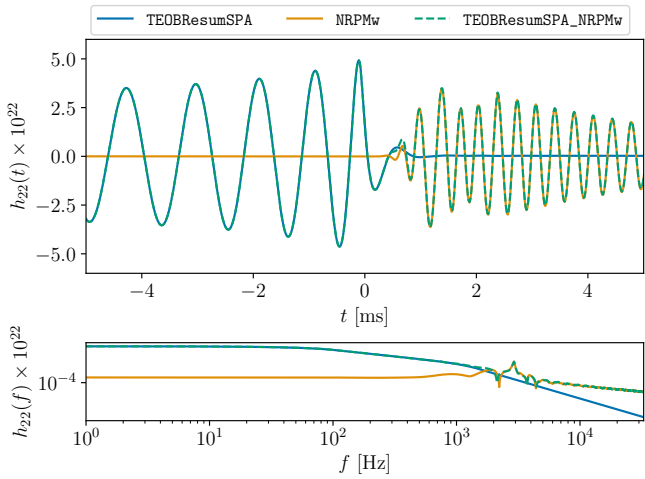


FIG. 1. Attachment between **TEOBResumSPA** and **NRPMw** for a GW template of non-spinning binary with  $m_1 = 1.5 M_\odot$ ,  $m_2 = 1.4 M_\odot$ ,  $\Lambda_1 = 400$ ,  $\Lambda_2 = 600$  and  $D_L = 40$  Mpc. Since the model is defined in the frequency domain, we obtain  $h_{22}(t)$  by performing an inverse FFT of  $h_{22}(f)$ .

the related theoretical uncertainties. **NRPMw** is parameterized by two additional sets of degrees of freedom (see Paper I for a detailed discussion). The PM parameters  $\theta_{\text{PM}}^{\text{free}} = \{\phi_{\text{PM}}, t_c, \alpha_{\text{drift}}\}$  correspond to: the PM phase-shift  $\phi_{\text{PM}}$  that identifies the phase discontinuity after merger; the time of collapse  $t_c$  that characterizes the collapse of the remnant into BH; and the frequency drift  $\alpha_{\text{drift}}$  that accounts for linear evolution of the dominant  $f_2$  component.

## II. METHOD

### A. Waveform model

In Paper I we introduced the PM **NRPMw** waveform, which can be employed to extend in the kiloHertz regime the existing frequency-domain approximants for GW signals from BNS mergers. For our studies, we resort to the EOB model **TEOBResumS** [72, 75, 76], in its frequency domain formulation, **TEOBResumSPA** [73, 77], for the representation of the IM part and present here the full spectrum template **TEOBResumSPA\_NRPMw**.

We attach the EOB model for the IM to the PM **NRPMw** template, focusing on the dominant (2, 2) mode. The information required to perform the attachment of **NRPMw** with **TEOBResumSPA** is the time and the phase at merger, respectively  $t_{\text{mrg}}$  and  $\phi_{\text{mrg}}$ . These data can be extracted from the EOB IM waveform. Then, resorting linear properties of the Fourier transform, the inspiral-merger-postmerger (IMPM) waveform can be computed as the sum of the pre-merger template  $h_{\text{EOB}}$  and the PM

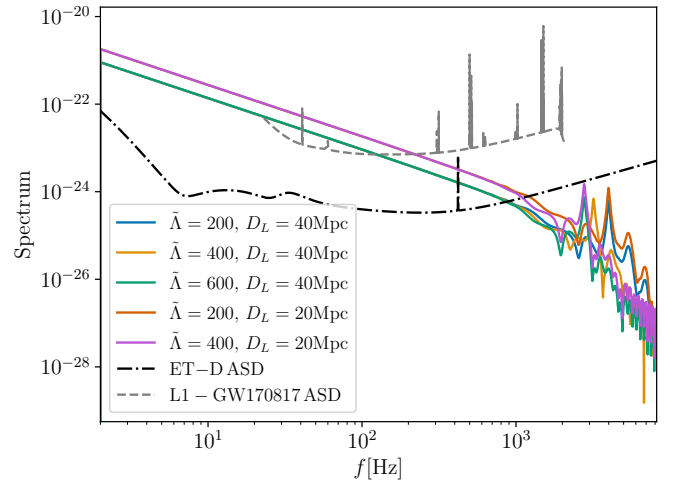


FIG. 2. Amplitude spectral density (ASD) of ET in configuration D [1, 2] (in black) and comparison with ASD of LIGO L1 detector, relative to GW170817 event [78] (in grey), to show the improvement in the detection of GW signals with XG detectors. The solid colored lines represent five exemplary BNS waveform spectra with **TEOBResumSPA\_NRPMw** template for  $M = 1.24 M_\odot$ ,  $q = 1$ , varying  $\tilde{\Lambda}$  and  $D_L$  as indicated in the legend.

one  $h_{\text{PM}}$  in the frequency-domain,

$$h_{\text{IMPM}}(f) = h_{\text{EOB}}(f) + h_{\text{PM}}(f) e^{-2\pi i f t_{\text{mrg}} + \phi_{\text{mrg}}}, \quad (7)$$

where  $h_{\text{PM}}(f)$  is taken such that its reference time and phase are vanishing.

Figure 1 illustrates an example of such an attachment procedure for a representative configuration with  $M = 2.9 M_\odot$ ,  $q = 1.072$ ,  $\Lambda_1 = 400$  and  $\Lambda_2 = 600$ . As shown, the **TEOBResumSPA\_NRPMw** waveform (dashed line) accurately reproduces the IM dynamics as described by the **TEOBResumSPA** template, as well as the PM segment following **NRPMw**. The attachment occurs after the merger, with the adoption of the phase from the EOB model, according to Eq. (7). To guarantee a smooth transition, the fusion wavelet, *i.e.* the portion of the **NRPMw** waveform between the merger time (as predicted by **TEOBResumSPA**) and  $t_0$ , defined as the first amplitude's minimum after the merger (See Paper I), is used to perform a continuous attachment of the PM with the IM. Consequently, this segment is not compatible with either model.

We also validate the model against six NR simulations that are not included in the calibration set of **NRPMw**, finding that the model is 89 – 95% faithful to NR when considering the full spectrum of frequencies and the ET-D sensitivity curve [1, 2]. More details on the IMPM model and its validation can be found in Appendix A.

## B. Inference

We perform Bayesian parameter estimation (PE) experiments by injecting and analyzing mock zero-noise BNS signals with XG detectors. We employ the power spectral density (PSD) curve of the ET detector, as reported in Fig. 2, in configuration D [1, 2], *i.e.* an equilateral triangular shape with 10 km long arms. We simulate both IM-only and IMPM waveforms and recover them using the same model employed for the injection, `TEOBResumSPA` and `TEOBResumSPA_NRPMw` respectively.

Bayesian inference is performed with the parallel `bajes` pipeline [79]. In order to efficiently explore the parameter space and compute the evidence, we utilize nested sampling algorithm [80–82] as implemented in the `dynesty` library [83] with a minimum of 2048 live points.

Bayesian analysis is based on the evaluation of the likelihood function (See Appendix B 1 for additional details), which is the most computationally expensive part. To speed up the computations, we make use of the relative binning technique [84, 85] in the IM part. Relative binning consists in the precomputation of frequency-binned overlap of a fiducial waveform with the data, since the ratio of neighboring waveforms in frequency domain is smooth in the inspiral part. In particular, for the IM-only PEs we employ the relative binning method for the whole frequency range of the integration. For the IMPM cases, we utilize relative binning only up to a cutoff frequency  $f_{\text{cut}} = 2048$  Hz and we perform a normal Bayesian PE without speed up after the cutoff frequency. The two likelihoods are then combined by summing their respective contributions:

$$\log p(\mathbf{d}|\boldsymbol{\theta}, H_S) = \log p(\mathbf{d}_{\text{IM}}|\boldsymbol{\theta}, H_{\text{IM}}^{\text{RB}}) + \log p(\mathbf{d}_{\text{PM}}|\boldsymbol{\theta}, H_{\text{PM}}). \quad (8)$$

where  $\log p(\mathbf{d}_{\text{IM}}|\boldsymbol{\theta}, H_{\text{IM}}^{\text{RB}})$  is the likelihood evaluated in the IM portion of the spectrum with relative binning, while  $\log p(\mathbf{d}_{\text{PM}}|\boldsymbol{\theta}, H_{\text{PM}})$  is evaluated in the high-frequency section, *i.e.* with `NRPMw`. For further explanation of the relative binning implementation and a discussion of the approximations used, we refer to Appendix B 2.

## C. EoS constraints from quasi-universal relations

Given an estimation of the intrinsic BNS parameters, we show how XG detectors can enable precise constraints on the EoS of NSs. Inference of IM delivers posteriors of the masses of the compact objects and of the tidal polarizability parameters. The information contained in the IMPM signals, instead, allows to go beyond  $m_i$  and  $\Lambda_i$  and probe high-density NS properties. Breschi *et al.* [15] combined the Fisher matrix approach in the IM part with the Bayesian analysis of the PM in order to obtain a tighter constraint on the mass-radius relation. Here we perform a full spectrum Bayesian PE, aiming to obtain more reliable inference, particularly in the high-density

regime. The resulting pipeline constrains different quantities of interest in EoS modeling and is described in what follows.

The first step is to map the posteriors for the total mass and the peak PM frequency  $f_2$  into posteriors of maximum density  $\rho_{\text{max}}^{\text{TOV}}$  and radius at the maximum mass  $R_{\text{max}}^{\text{TOV}}$ , using the NR phenomenological relations [15, 86]:

$$\rho_{\text{max}}^{\text{TOV}} = \frac{a_0 c^6}{G^3 M^2} \left[ 1 + a_1 \left( \frac{c^3}{\pi G M f_2} \right)^{1/6} \right], \quad (9)$$

with  $(a_0, a_1) = (0.135905, -0.59506)$  and

$$R_{\text{max}}^{\text{TOV}}/M = (5.81 \pm 0.13) - (123.4 \pm 7.2) M f_2 + (1121 \pm 99) (M f_2)^2. \quad (10)$$

Subsequently, we use a sample of two millions EoSs from Godzieba *et al.* [87] generated under minimal assumptions, *i.e.* general relativity, causality, the maximum NS mass above the maximum NS mass from pulsar observations,  $M_{\text{max}}^{\text{TOV}} > 1.97 M_{\odot}$  [88], and consistent with the upper bound on the reduced tidal parameter  $\tilde{\Lambda}$  from GW170817 [17, 19, 89]. We reweigh the EoS sample with the posteriors of the masses, the reduced tidal parameter,  $\rho_{\text{max}}^{\text{TOV}}$  and  $R_{\text{max}}^{\text{TOV}}$ , employing `emcee` sampler [90]. This allows us to place constraints not only on the NS mass-radius diagram, but also to determine the 90% credibility region for the tidal deformability curve  $\Lambda(M)$  and on the pressure-density relation  $p(\rho)$ . Specifically, from the EoS sampling we obtain a distribution of EoSs that most closely resemble the one used for the injection. For each sampled EoS, we compute the relations between the mass and the radius of the star and between the tidal polarizability parameter and the mass, yielding a 90% confidence interval (CI) on the  $M(R)$  and the  $\Lambda(M)$  curve, respectively. Using the same EoS distribution we solve the Tolmann-Oppenheimer-Volkoff (TOV) equations to determine the corresponding pressure-density relation, from which we derive the 90% confidence region for the  $p(\rho)$  curve.

The maximum mass of non-rotating NSs,  $M_{\text{max}}^{\text{TOV}}$ , is a crucial parameter for constraining the mass-radius diagram and consequently the EoS. Additionally, it is also essential for the determination of the probability of prompt collapse. Specifically, PC is expected to occur when the total mass of the system exceeds a threshold mass, which is related through phenomenological relations to  $M_{\text{max}}^{\text{TOV}}$  [64, 65]:

$$M_{\text{thr}} = k_{\text{thr}}(C_{\text{max}}) M_{\text{max}}^{\text{TOV}}, \quad (11)$$

where  $k_{\text{thr}}(C_{\text{max}})$  is a function of the compactness of the star. The values of  $C_{\text{max}}$  and  $M_{\text{max}}^{\text{TOV}}$  come from the EoS sampling as presented above. In our analysis we adopt the updated fits for  $k_{\text{thr}}$  of [66], which were obtained for equal-mass binaries. Peregó *et al.* [67] provide a more general characterization with mass ratio effects and show that the latter give corrections compatible with the fit

uncertainty down to mass ratios  $q \lesssim 1.4-1.5$  (depending on EoS). For larger mass ratio PC is driven by accretion effects of the secondary stars to the primary and require a more sophisticated parametrization. Empirical models for the threshold mass can be obtained also in those cases by considering, for example, the EoS incompressibility parameter at extreme densities. Typical deviations from the equal-mass relation are up to  $\sim 20\%$  for mass ratios  $q \sim 2$ .

In our PC analyses, we consider equal-mass binaries and determine the 90% CI of the maximum mass  $M_{\text{max}}^{\text{TOV}}$  and the corresponding radius  $R_{\text{max}}^{\text{TOV}}$  of the NS from the mass-radius diagram and insert them in Eq. (11). We then calculate the probability of PC as

$$P_{\text{PC}} = P(M > M_{\text{thr}}|d), \quad (12)$$

as proposed by Agathos et al. [70].

In addition, the presence of PC can also be statistically evaluated by computing the Bayes' factor (BF) between models that assume either a PC to a BH or the formation of a NS remnant [13] (see Appendix B 1 for details on BF calculation). An alternative method to assess the occurrence of PC is to estimate the collapse time,  $t_c$ , to a BH, which is a parameter introduced in NRPMw waveforms. For practical purposes we assume that a system promptly collapses to a BH if  $t_c < t_c^{\text{thr}} = 2$  ms. This threshold just serves as an upper limit for the PC timescale; since a proper definition of PC requires inspection of the bulk merger dynamics [91].

### III. RESULTS

#### A. Inspiral-merger

In this section we consider nine injection-recovery PEs with TEOBResumSPA. We vary the initial frequency of the analyses and the luminosity distance of the binaries, comparing the recovered parameters with the injected ones. This approach allows us to investigate how constraints on various parameters depend on the different SNRs of the signals.

We generate artificial data in the frequency domain, using the triangular, triple-interferometer ET detector [4, 93, 94], with ET-D sensitivity [1, 2] and a sampling rate of 4096 Hz. The sky location corresponds to the optimal location for the ET detector  $\{\alpha = 2.64, \delta = 0.762\}$  and the binaries are oriented with  $\iota = 0$  and  $\psi = 0$ . The injections are performed in zero-noise, including only the dominant (2,2) mode. The injected strain is analyzed in the frequency domain from  $f_0$  to 2048 Hz, where  $f_0 \in [2, 5, 10, 20]$  Hz. We set the priors for chirp mass  $\mathcal{M} \in [0.8, 1.5]M_{\odot}$ , for mass ratio  $q \in [1, 2]$  and for the tidal polarizability parameters  $\Lambda_{1,2} \in [0, 3000]$ . The spins are aligned with the orbital angular momentum, with an isotropic prior  $\chi_{1,2} \in [-0.05, 0.05]$  for the  $z$ -component. Finally, for the luminosity distance we

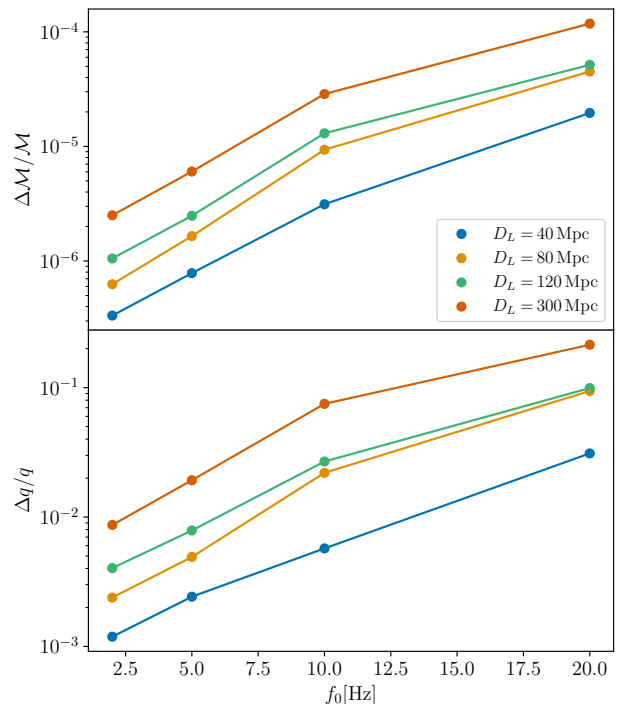


FIG. 3. Relative precision on chirp mass (top) and mass ratio (bottom) with respect to the different initial frequencies for a non-spinning BNS with  $\mathcal{M} = 1.1976917M_{\odot}$ ,  $q = 1.5$ ,  $\tilde{\Lambda} = 488$ , at different luminosity distances. A lower initial frequency or a closer source leads to improved precision in both the chirp mass and the mass ratio estimations.

employ volumetric priors  $D_L \in [10, 150]$  Mpc, except when the injected luminosity distance is 300 Mpc, where we use  $D_L \in [200, 400]$  Mpc. We marginalize over reference phase.

#### 1. Source parameters

Figure 3 shows the relative precision on chirp mass and mass ratio calculated as

$$\frac{\Delta x}{x} = \frac{x_{95\%} - x_{5\%}}{x_m}, \quad (13)$$

where  $x_m$  is the median value and  $x_{95\%}$  ( $x_{5\%}$ ) corresponds to the 95th (5th) percentile of the posterior distribution of the parameter  $x$ . The injected GW signals correspond to non-spinning BNS with  $\mathcal{M} = 1.1976917M_{\odot}$ ,  $q = 1.5$  and  $\tilde{\Lambda} = 488$ . We vary the luminosity distance in  $[40, 80, 120, 300]$  Mpc. The precision on both  $\mathcal{M}$  and  $q$  increases as the distance of the source decreases, since the SNR is higher. Similarly, keeping a fixed luminosity distance, the precision increases as the initial frequency

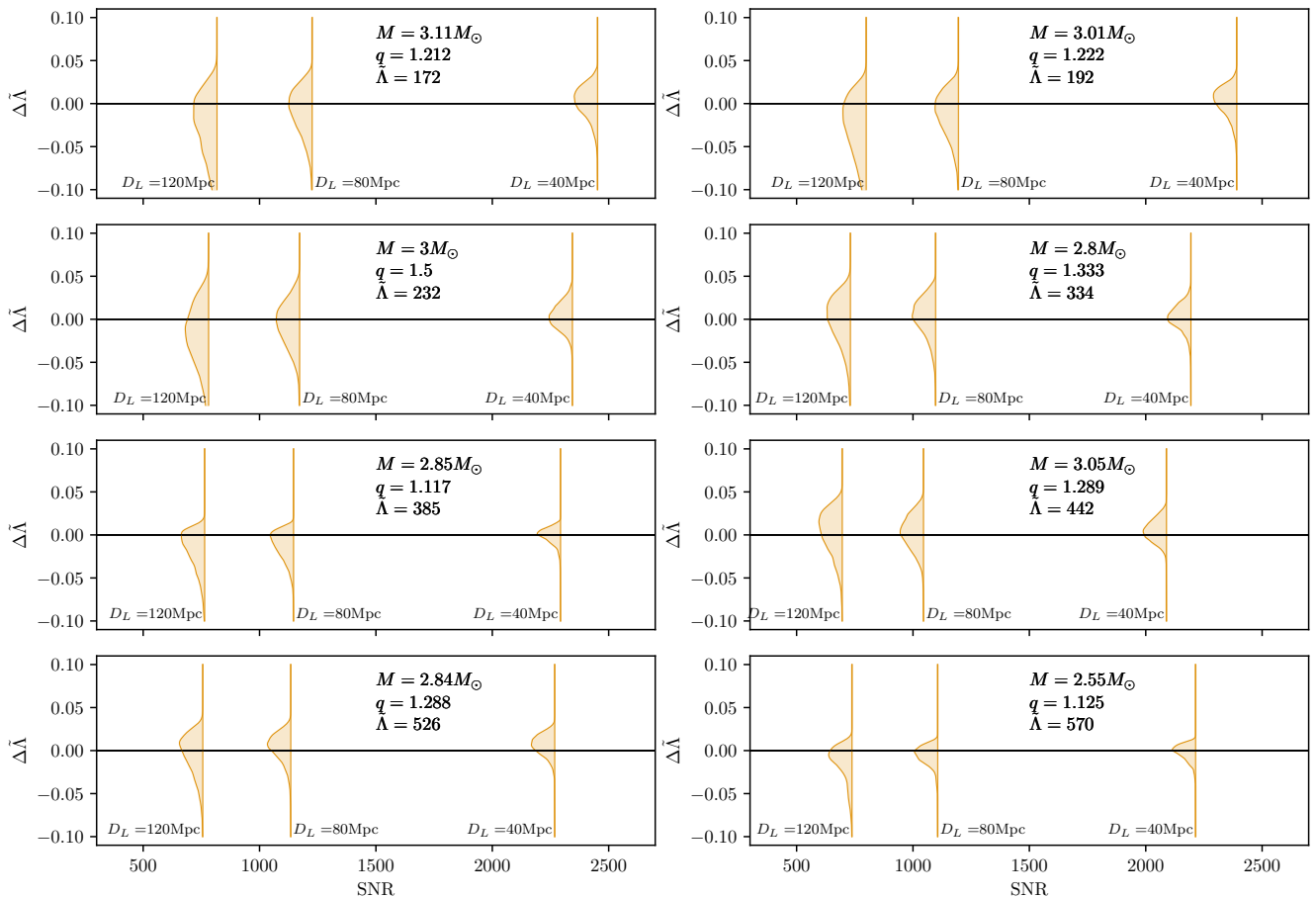


FIG. 4. Posterior distributions for reduced tidal parameter  $\tilde{\Lambda}$  with respect to SNR, varying the injected luminosity distances, for eight fiducial binaries. The initial frequency is kept fixed to  $f_0 = 5$  Hz. As the SNR increases, *i.e.* the luminosity distance decreases, the width of the distribution of  $\tilde{\Lambda}$  shrinks.

$f_0$  of the analysis decreases, *e.g.* at  $D_L = 300$  Mpc, decreasing the frequency from 20 Hz to 5 Hz, the precision on the measurement of both chirp mass and mass ratio improves of about one order of magnitude.

Figure 4 shows the distributions of the differences between the recovered and the injected values of the reduced tidal parameter,

$$\frac{\Delta\tilde{\Lambda}}{\tilde{\Lambda}} = \frac{|\tilde{\Lambda}_{\text{rec}} - \tilde{\Lambda}_{\text{inj}}|}{\tilde{\Lambda}_{\text{inj}}}, \quad (14)$$

with respect to the SNR, for eight different binaries. As the SNR increases, that is when the luminosity distance decreases, the width of the distribution shrinks, meaning that the measurement of  $\tilde{\Lambda}$  is more precise. This is mostly due to the improvement in the chirp mass and mass ratio discussed above. We run the same test fixing the luminosity distance and varying the initial frequencies of the analyses. The results are presented in Fig. 5. We obtain a similar result as before: as the SNR increases, namely as the initial frequency decreases, it is possible to have a better estimation on the value of  $\tilde{\Lambda}$ ,

*e.g.* of about a factor two, when the initial frequency changes from 20 to 5 Hz. Reducing the luminosity distance from 120 Mpc to 40 Mpc, instead, improves the precision on the reduced tidal parameters by a factor between two and three. At the same time, we notice that having a larger luminosity distance, *i.e.* 80 Mpc, but a smaller initial frequency, *i.e.* 5 Hz, enhances the precision in the measurement of all the parameters with respect to a closer source ( $D_L = 40$  Mpc) at  $f_0 = 20$  Hz, even if the SNR is higher in the latter case. Thus, decreasing the initial frequency is an effective strategy to achieve better constraints in the estimation of the binary parameters.

Table I presents the recovered median values with the 90% confidence regions for the inferred parameters. In addition to the consideration above about the chirp mass and the mass ratio, as the initial frequency decreases from 20 Hz to 2 Hz, the precision on the estimation of the reduced tidal parameter increases of about a factor two and the precision on the effective spin of one order of magnitude. The precision of the luminosity distance and of the inclination, instead, is comparable for the different cases and the inferred values are not always compatible

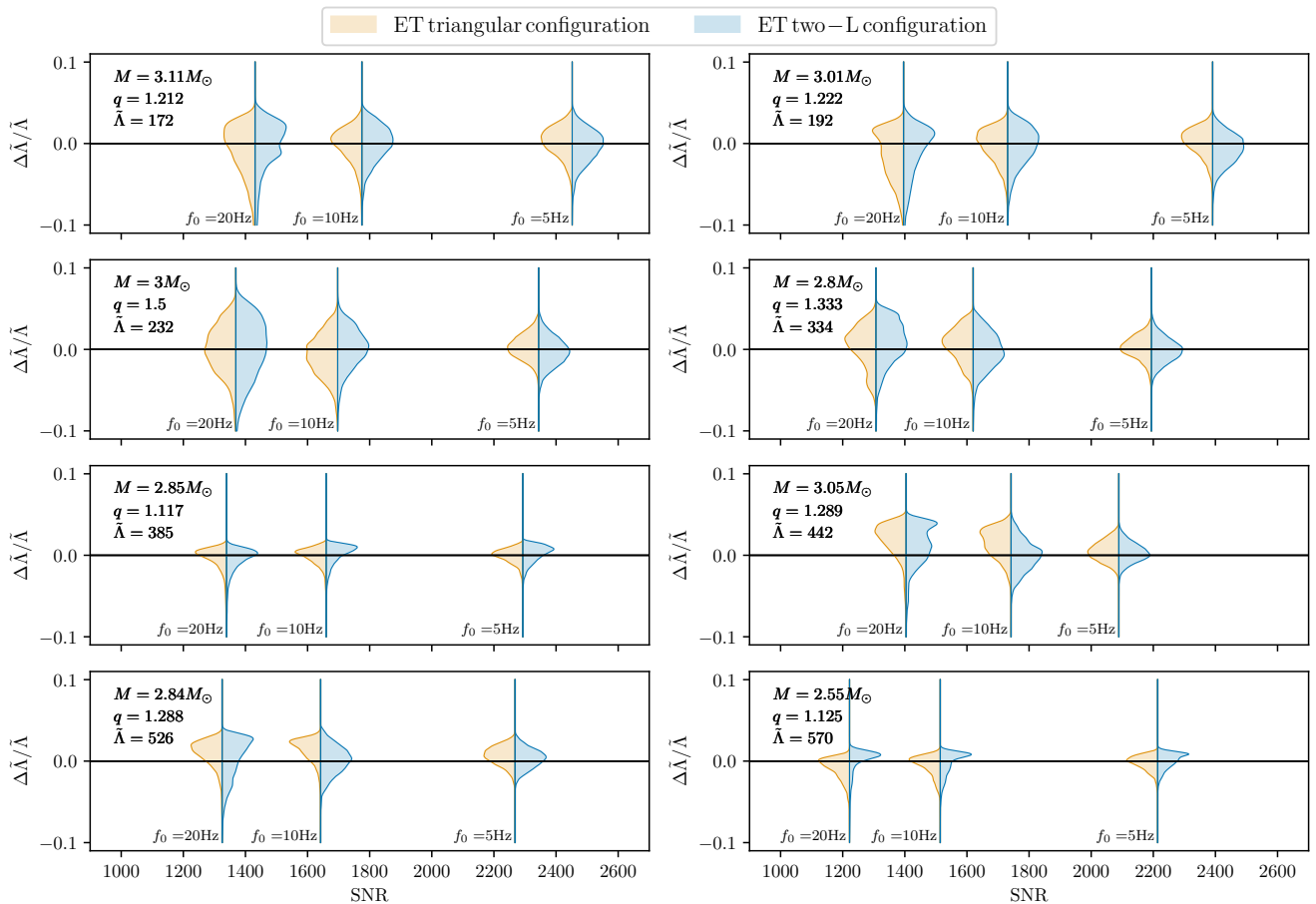


FIG. 5. Posterior distributions for reduced tidal parameter  $\tilde{\Lambda}$  with respect to SNR, varying the initial frequencies of the detection, for eight fiducial binaries. The luminosity distance is kept fixed to  $D_L = 40$  Mpc. As the SNR increases, *i.e.* the initial frequency decreases, the width of the distribution of  $\tilde{\Lambda}$  shrinks. Two different configurations of ET, triangular [1, 2] in orange and two-L [92] in blue, give comparable results.

with the injected ones. This is due to the known degeneracy between distance and inclination, which arises when considering waveforms constructed only with the  $(2, \pm 2)$  modes [95]. Despite this, our results of the precision of the luminosity distance are consistent with those reported in [96].

In Table I and in Table IV of Appendix C we also report the recovered values of the asymmetric tidal parameter  $\delta\tilde{\Lambda}$ . The estimation on this parameter carries substantial uncertainties, in some case larger than 100%. The trend in the improvement of its precision follows the same behavior discussed above for the reduced tidal parameter. We notice that, when the SNR is sufficiently high, *i.e.*  $\text{SNR} \gtrsim 1500$  for  $q > 1.2$ , the recovered values of  $\delta\tilde{\Lambda}$  deviate significantly from zero, indicating a measurable asymmetry in the tidal polarizability parameters. Furthermore, the joint estimation of  $\delta\tilde{\Lambda}$  and  $\tilde{\Lambda}$  leads to constraints on the individual tidal polarizability parameters. In few cases, when the mass ratio is  $q \gtrsim 1.289$  and the SNR has the highest value, *i.e.*  $f_0 = 5$  Hz and  $D_L = 40$  Mpc, we notice that both the posterior distribu-

tions of  $\Lambda_1$  and  $\Lambda_2$  are not compatible with zero, enabling us to confidently identify the source as a BNS merger. However, in all the other cases, the posterior distribution of  $\Lambda_1$  remains compatible with zero, preventing us from discarding the BH-NS hypothesis.

## 2. Comparison of ET configurations

In Figure 5 we compare two different configurations of ET, the triangular one [1, 2], described in Sec. II B and a two-L configuration [92], where the first detector is located in the Meuse-Rhine region and the second one in Sardinia, with the same sensitivity as the triangular one [1, 2] and a relative orientation between the two detectors of  $45^\circ$ . We find that the posterior distributions of  $\tilde{\Lambda}$  for the two configurations are comparable. Our results are in line with [97].

We then perform a comparison between the two different configurations of ET for what concerns the recovery of the extrinsic parameters, *i.e.* right ascension  $\alpha$ , decli-

TABLE I. Summary of the PEs with **TEOBResumSPA** for a BNS with  $\mathcal{M} = 1.1976917M_{\odot}$ ,  $q = 1.5$ ,  $\tilde{\Lambda} = 488$ ,  $\delta\tilde{\Lambda} = -60$ ,  $\chi_{\text{eff}} = 0$ ,  $\iota = 0$ . The first three columns report the injected luminosity distance, the initial frequency of the analyses and the SNR of the injected data; the last seven columns report the recovered values, with the median of the posterior distributions and the 90% CIs.

Injected properties			Recovered values						
$D_L$ [Mpc]	$f_0$ [Hz]	SNR	$\mathcal{M}$ [ $M_{\odot}$ ]	$q$	$\tilde{\Lambda}$	$\delta\tilde{\Lambda}$	$\chi_{\text{eff}}$	$D_L$ [Mpc]	$\iota$
40	2	2261	$1.1976917^{+0.0000002}_{-0.0000002}$	$1.500^{+0.002}_{-0.002}$	$490^{+9}_{-9}$	$-50^{+30}_{-30}$	$-0.0001^{+0.0001}_{-0.0001}$	$38.5^{+1.0}_{-0.8}$	$0.26^{+0.07}_{-0.13}$
	5	2228	$1.1976917^{+0.0000005}_{-0.0000005}$	$1.500^{+0.004}_{-0.004}$	$488^{+10}_{-10}$	$-70^{+20}_{-20}$	$0.0000^{+0.0002}_{-0.0002}$	$40.00^{+0.01}_{-0.01}$	$0.02^{+0.01}_{-0.01}$
	10	1613	$1.197691^{+0.000002}_{-0.000002}$	$1.498^{+0.011}_{-0.009}$	$490^{+12}_{-14}$	$-60^{+30}_{-30}$	$-0.0001^{+0.0009}_{-0.0007}$	$40.01^{+0.02}_{-0.01}$	$0.02^{+0.01}_{-0.01}$
	20	1301	$1.19769^{+0.00001}_{-0.00001}$	$1.50^{+0.04}_{-0.05}$	$490^{+30}_{-20}$	$-60^{+70}_{-30}$	$-0.0002^{+0.0030}_{-0.0040}$	$37.7^{+0.9}_{-0.8}$	$0.33^{+0.06}_{-0.08}$
80	2	1130	$1.1976917^{+0.0000004}_{-0.0000004}$	$1.500^{+0.003}_{-0.004}$	$490^{+20}_{-20}$	$-40^{+65}_{-40}$	$-0.0001^{+0.0002}_{-0.0003}$	$76^{+2}_{-3}$	$0.30^{+0.09}_{-0.13}$
	5	1114	$1.1976915^{+0.0000010}_{-0.0000010}$	$1.499^{+0.008}_{-0.007}$	$490^{+30}_{-20}$	$-40^{+80}_{-50}$	$-0.0001^{+0.0005}_{-0.0005}$	$76^{+3}_{-2}$	$0.31^{+0.09}_{-0.14}$
	10	806	$1.197690^{+0.000005}_{-0.000006}$	$1.49^{+0.03}_{-0.03}$	$500^{+50}_{-30}$	$-40^{+160}_{-50}$	$-0.0005^{+0.0020}_{-0.0020}$	$75^{+3}_{-3}$	$0.33^{+0.09}_{-0.14}$
	20	650	$1.19769^{+0.00002}_{-0.00003}$	$1.49^{+0.06}_{-0.14}$	$500^{+90}_{-40}$	$-30^{+220}_{-60}$	$-0.0007^{+0.0060}_{-0.0110}$	$75^{+3.0}_{-3}$	$0.36^{+0.09}_{-0.13}$
120	2	754	$1.1976916^{+0.0000006}_{-0.0000006}$	$1.498^{+0.006}_{-0.006}$	$500^{+30}_{-30}$	$0^{+110}_{-90}$	$-0.0000^{+0.0007}_{-0.0006}$	$113^{+5}_{-4}$	$0.3^{+0.1}_{-0.2}$
	5	743	$1.197692^{+0.000001}_{-0.000002}$	$1.50^{+0.01}_{-0.01}$	$490^{+40}_{-20}$	$-30^{+150}_{-70}$	$-0.0001^{+0.0008}_{-0.0010}$	$113^{+4}_{-5}$	$0.3^{+0.1}_{-0.1}$
	10	538	$1.197689^{+0.000008}_{-0.000008}$	$1.49^{+0.04}_{-0.04}$	$510^{+60}_{-50}$	$0^{+170}_{-100}$	$-0.001^{+0.003}_{-0.003}$	$112^{+6}_{-5}$	$0.4^{+0.1}_{-0.2}$
	20	434	$1.19768^{+0.00002}_{-0.00004}$	$1.46^{+0.09}_{-0.14}$	$530^{+70}_{-70}$	$20^{+200}_{-110}$	$-0.003^{+0.008}_{-0.011}$	$111^{+6}_{-5}$	$0.4^{+0.1}_{-0.2}$
300	2	301	$1.197692^{+0.000002}_{-0.000002}$	$1.50^{+0.01}_{-0.01}$	$510^{+60}_{-50}$	$80^{+160}_{-160}$	$-0.0004^{+0.0010}_{-0.0013}$	$270^{+10}_{-10}$	$0.4^{+0.1}_{-0.2}$
	5	297	$1.197691^{+0.000003}_{-0.000004}$	$1.49^{+0.02}_{-0.03}$	$530^{+50}_{-70}$	$100^{+130}_{-180}$	$-0.0002^{+0.0020}_{-0.0020}$	$280^{+20}_{-20}$	$0.4^{+0.2}_{-0.2}$
	10	215	$1.19769^{+0.00001}_{-0.00002}$	$1.49^{+0.07}_{-0.11}$	$500^{+100}_{-70}$	$20^{+210}_{-130}$	$-0.0005^{+0.0050}_{-0.0090}$	$270^{+20}_{-20}$	$0.4^{+0.1}_{-0.3}$
	20	173	$1.19768^{+0.00008}_{-0.00007}$	$1.4^{+0.2}_{-0.3}$	$540^{+70}_{-110}$	$100^{+120}_{-220}$	$-0.005^{+0.021}_{-0.020}$	$270^{+20}_{-20}$	$0.4^{+0.2}_{-0.2}$

nation  $\delta$ , inclination  $\iota$  and luminosity distance  $D_L$ . Figure 6 shows the posterior distributions of the difference between the recovered and the injected values for the extrinsic parameters, since for each detector we use the best location. We notice that the 90% confidence regions are comparable for the two configurations for all the parameters, except for the declination, which is better recovered in the case of the two-L configuration.

Branchesi et al. [92], Begoni et al. [98] and Puecher et al. [97] compared various ET geometries using a Fisher matrix approach in the former cases and a Bayesian PE in the latter. They all concluded that an improvement in the precision on the inference of the source parameters comes primarily from the arms length, while changing shape or alignment of the detectors plays a minimal role in the accuracy increase. Additionally, Branchesi et al. [92] found that the estimation of the source parameters is comparable for the two configurations we considered, while the triangular performs better in the estimation of the inclination angle. Regarding the angular localization, their results indicate that the two-L is better compared to the triangular one. This improvement is attributed to the ability of the two-L setup to partially triangulate, thanks to its longer baseline. These findings are compatible with our results.

## B. Inspiral-merger-postmerger

This section is dedicated to the analysis of IMPM injection-recovery PEs. We employed the complete

**TEOBResumSPA\_NRPMw** template for the injections of GWs from different binaries, *i.e.* with different EoSs. As in the IM-only case, the detector used is ET, with triangular shape and ET-D sensitivity [1, 2]. The sky location is the same as in III A and the luminosity distance is 40 Mpc. The sampling rate is 16384 Hz and the analyses are performed in the frequency range  $f \in [20, 8192]$  Hz. The priors for chirp mass are  $\mathcal{M} \in [0.8, 2] M_{\odot}$ , for mass ratio  $q \in [1, 4]$ , for the tidal polarizability parameters  $\Lambda_{1,2} \in [0, 4000]$  and for the luminosity distance are volumetric  $D_L \in [10, 1000]$  Mpc. We perform the inference under the assumption of non-spinning binaries and we keep all the other extrinsic parameters fixed to the injected values. We add the recalibration parameters  $\delta_{\text{fit}}$  to account for intrinsic errors of the calibrated formulae (see Paper I).

Figure 7 displays an example of posterior distributions for the LS220 binary of Table II with  $\mathcal{M} = 1.223692 M_{\odot}$ . We compare between IM and IMPM recoveries. The posteriors distributions are, in both cases, correctly centered on the injected values (black lines) and they are similar. We observe that the inclusion of the PM does not significantly improve the constraints on chirp mass, mass ratio and tidal polarizability parameter compared to the IM-only PE. This outcome is primarily due to the dominant contribution of the IM segment, which exhibits a SNR on the order of  $10^3$ , whereas the SNR of the PM is only on the order of ten (the SNR threshold for detectability of the PM is 7 [Paper II]). Nevertheless, having a model that incorporates the PM remains essential for distinguishing between the characteristic PM features of a NS remnant

TABLE II. Summary of the PEs with **TEOBResumSPA** for IM and **TEOBResumSPA\_NRP Mw** for IMPM case. The first five columns report the injected parameters, included the EoS used; the central six columns report the recovered values, with the median of the posterior distributions and the 90% CIs and the last column displays the BFs, with statistical uncertainties as in [99].

Injected properties					Recovered values IM			Recovered values IMPM			$\log \mathcal{B}_{\text{IM}}^{\text{IMPM}}$
morph.	$\mathcal{M}$ [ $M_{\odot}$ ]	$q$	$\tilde{\Lambda}$	SNR	$\mathcal{M}$ [ $M_{\odot}$ ]	$q$	$\tilde{\Lambda}$	$\mathcal{M}$ [ $M_{\odot}$ ]	$q$	$\tilde{\Lambda}$	
DD2	1.339520	1	403	1427	$1.339519^{+0.000001}_{-0.000001}$	$1.013^{+0.015}_{-0.012}$	$400^{+4}_{-6}$	$1.339519^{+0.000001}_{-0.000001}$	$1.016^{+0.012}_{-0.011}$	$400^{+4}_{-6}$	$32.29^{+0.47}_{-0.47}$
BHBA $\phi$	1.319184	1	434	1409	$1.319184^{+0.000001}_{-0.000001}$	$1.013^{+0.014}_{-0.012}$	$431^{+4}_{-6}$	$1.319184^{+0.000001}_{-0.000001}$	$1.016^{+0.011}_{-0.011}$	$431^{+5}_{-6}$	$31.98^{+0.47}_{-0.47}$
DD2	1.522426	1	178	1583	$1.522425^{+0.000001}_{-0.000001}$	$1.011^{+0.013}_{-0.010}$	$177^{+2}_{-3}$	$1.522425^{+0.000001}_{-0.000002}$	$1.016^{+0.012}_{-0.011}$	$176^{+3}_{-3}$	$29.54^{+0.48}_{-0.48}$
LS220	1.170202	1	703	1278	$1.170202^{+0.000001}_{-0.000001}$	$1.015^{+0.014}_{-0.013}$	$699^{+6}_{-8}$	$1.170202^{+0.000001}_{-0.000001}$	$1.015^{+0.012}_{-0.012}$	$699^{+7}_{-8}$	$24.99^{+0.47}_{-0.47}$
DD2	1.315304	1.289	442	1405	$1.315304^{+0.000002}_{-0.000002}$	$1.289^{+0.002}_{-0.002}$	$443^{+12}_{-14}$	$1.315304^{+0.000002}_{-0.000002}$	$1.290^{+0.002}_{-0.002}$	$440^{+12}_{-13}$	$22.25^{+0.48}_{-0.48}$
SLy	1.175243	1	394	1466	$1.175243^{+0.000001}_{-0.000001}$	$1.014^{+0.014}_{-0.012}$	$390^{+5}_{-6}$	$1.175243^{+0.000001}_{-0.000001}$	$1.014^{+0.011}_{-0.011}$	$392^{+4}_{-5}$	$19.39^{+0.48}_{-0.48}$
BLh	1.227164	1	412	1329	$1.227163^{+0.000001}_{-0.000001}$	$1.012^{+0.015}_{-0.011}$	$409^{+5}_{-6}$	$1.227163^{+0.000001}_{-0.000001}$	$1.017^{+0.012}_{-0.012}$	$408^{+4}_{-6}$	$18.90^{+0.47}_{-0.47}$
DD2	1.043690	1	1638	1164	$1.043690^{+0.000000}_{-0.000001}$	$1.015^{+0.016}_{-0.013}$	$1631^{+9}_{-18}$	$1.043690^{+0.000001}_{-0.000001}$	$1.018^{+0.014}_{-0.013}$	$1629^{+10}_{-17}$	$16.72^{+0.46}_{-0.46}$
BLh	1.341381	1	222	1429	$1.341381^{+0.000001}_{-0.000001}$	$1.012^{+0.013}_{-0.011}$	$220^{+3}_{-4}$	$1.341380^{+0.000001}_{-0.000001}$	$1.013^{+0.012}_{-0.012}$	$221^{+3}_{-4}$	$15.16^{+0.48}_{-0.48}$
SFHo	1.130733	1	538	1243	$1.130733^{+0.000000}_{-0.000001}$	$1.014^{+0.015}_{-0.012}$	$534^{+6}_{-8}$	$1.130732^{+0.000001}_{-0.000001}$	$1.017^{+0.012}_{-0.012}$	$534^{+6}_{-8}$	$15.05^{+0.46}_{-0.46}$
BLh	1.239566	1	385	1339	$1.239565^{+0.000001}_{-0.000001}$	$1.117^{+0.004}_{-0.004}$	$385^{+7}_{-12}$	$1.239565^{+0.000001}_{-0.000001}$	$1.117^{+0.004}_{-0.003}$	$385^{+6}_{-9}$	$14.36^{+0.47}_{-0.47}$
SFHo	1.273413	1	249	1369	$1.273412^{+0.000001}_{-0.000001}$	$1.013^{+0.014}_{-0.011}$	$247^{+3}_{-4}$	$1.273412^{+0.000001}_{-0.000001}$	$1.016^{+0.013}_{-0.012}$	$246^{+4}_{-5}$	$14.19^{+0.47}_{-0.47}$
SFHo	1.344787	1.212	172	1432	$1.344787^{+0.000002}_{-0.000002}$	$1.213^{+0.002}_{-0.002}$	$171^{+6}_{-9}$	$1.344787^{+0.000002}_{-0.000001}$	$1.213^{+0.002}_{-0.002}$	$171^{+5}_{-7}$	$13.94^{+0.48}_{-0.48}$
SLy	1.058974	1	743	1178	$1.058974^{+0.000000}_{-0.000001}$	$1.013^{+0.015}_{-0.012}$	$738^{+7}_{-10}$	$1.058974^{+0.000001}_{-0.000001}$	$1.018^{+0.012}_{-0.013}$	$737^{+7}_{-10}$	$12.99^{+0.46}_{-0.46}$
SLy	1.244295	1	264	1344	$1.244295^{+0.000001}_{-0.000001}$	$1.012^{+0.014}_{-0.011}$	$262^{+4}_{-4}$	$1.244295^{+0.000001}_{-0.000001}$	$1.016^{+0.013}_{-0.012}$	$261^{+4}_{-5}$	$12.89^{+0.47}_{-0.47}$
SLy	1.303371	1	191	1396	$1.303371^{+0.000001}_{-0.000001}$	$1.012^{+0.013}_{-0.011}$	$189^{+3}_{-4}$	$1.303370^{+0.000001}_{-0.000001}$	$1.015^{+0.012}_{-0.011}$	$189^{+3}_{-4}$	$12.51^{+0.47}_{-0.47}$
LS220	1.223692	1.287	525	1325	$1.223692^{+0.000001}_{-0.000002}$	$1.288^{+0.002}_{-0.002}$	$525^{+13}_{-16}$	$1.223692^{+0.000001}_{-0.000001}$	$1.288^{+0.002}_{-0.002}$	$525^{+11}_{-15}$	$12.22^{+0.47}_{-0.47}$
SLy	1.304020	1.222	192	1396	$1.304020^{+0.000001}_{-0.000002}$	$1.220^{+0.002}_{-0.002}$	$192^{+6}_{-9}$	$1.304020^{+0.000001}_{-0.000001}$	$1.220^{+0.002}_{-0.002}$	$192^{+5}_{-7}$	$9.78^{+0.48}_{-0.48}$
SLy	1.183075	1.257	365	1289	$1.183075^{+0.000001}_{-0.000001}$	$1.257^{+0.002}_{-0.002}$	$365^{+10}_{-14}$	$1.183075^{+0.000001}_{-0.000001}$	$1.257^{+0.002}_{-0.002}$	$363^{+11}_{-14}$	$8.91^{+0.47}_{-0.47}$
SFHo	1.339422	1	130	1427	$1.339422^{+0.000001}_{-0.000001}$	$1.012^{+0.013}_{-0.011}$	$129^{+3}_{-3}$	$1.339422^{+0.000001}_{-0.000001}$	$1.014^{+0.012}_{-0.011}$	$129^{+3}_{-3}$	$7.17^{+0.48}_{-0.48}$
2B	1.175243	1	126	1283	$1.175243^{+0.000001}_{-0.000001}$	$1.013^{+0.013}_{-0.011}$	$124^{+4}_{-4}$	$1.175243^{+0.000001}_{-0.000001}$	$1.013^{+0.013}_{-0.011}$	$124^{+4}_{-4}$	$-3.63^{+0.47}_{-0.47}$
DD2	1.522426	1	178	1583	$1.522425^{+0.000001}_{-0.000002}$	$1.015^{+0.013}_{-0.011}$	$177^{+2}_{-3}$	$1.522425^{+0.000001}_{-0.000002}$	$1.015^{+0.013}_{-0.011}$	$177^{+2}_{-3}$	$-5.84^{+0.47}_{-0.47}$
SLy	1.303371	1	191	1396	$1.303370^{+0.000001}_{-0.000001}$	$1.014^{+0.013}_{-0.011}$	$189^{+3}_{-4}$	$1.303370^{+0.000001}_{-0.000001}$	$1.014^{+0.013}_{-0.011}$	$189^{+3}_{-4}$	$-6.28^{+0.47}_{-0.47}$

and the case of a PC, by using BFs for model selection, as discussed below.

Figure 8 presents five illustrative recovered spectra, in which the injected waveforms are included within the 90% CIs of the reconstructed spectra. Particularly, both the inspiral part and the frequency of the peak of the PM,  $f_2$ , are well recovered with tight error bars for all the binaries, *i.e.* it is possible to obtain constraints on  $f_2$  for different EoSs with an uncertainty smaller than 8%. The high-frequency features and the region between the merger and the peak of the PM are consistent with the injection, but, in these cases, the 90% CI are broader, indicating lower precision on the detection compared to the inspiral segment. This reduced precision arises because the strain amplitude is about two orders of magnitude smaller and the detector sensitivity is lower in the high-frequency region.

In Table II we report the results of the PE analyses we performed. In all the cases we use both the IM waveform **TEOBResumSPA** and the IMPM waveform **TEOBResumSPA\_NRP Mw** for the recoveries. The inferred values for the two cases are comparable and always compat-

ible with the injected values. We compute the BFs as

$$\log \mathcal{B}_{\text{IM}}^{\text{IMPM}} = \log \frac{p(d|\text{IMPM})}{p(d|\text{IM})}, \quad (15)$$

where  $p(d|H)$  is the evidence. In the upper part of the Table the BFs are larger than zero, meaning that the IMPM model is preferred over the IM model. All the BF values are on the order of ten, whereas the associated uncertainties, estimated with the criterion introduced in [99], are on the order  $10^{-1}$ . This indicates a high degree of statistical confidence, supporting a clear detection of the presence of the PM. In the bottom part of the Table, instead, we test the ability of our pipeline to recover PC. The relative discussion is postponed to Sec. III D.

### C. EoS constraints

In this section we present the results of the EoS study enabled by our PE analyses. In particular EoS sampling can be performed starting from the results of the IM-only PEs, employing only the masses and the tidal polarizability parameters, or from the results of the PM, incorporating also the constraints from the quasi-universal

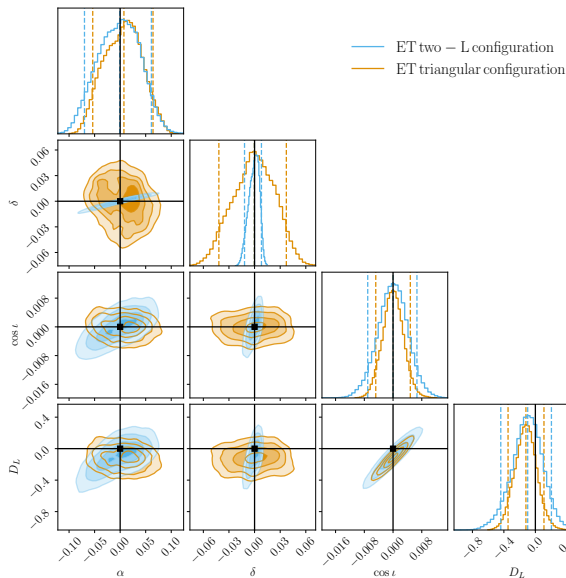


FIG. 6. Comparison of the posterior distributions for extrinsic parameters for two different ET configurations: triangular [1, 2] in orange and two-L [92] in blue. The injections have been performed with `TEOBResumSPA` template with  $\mathcal{M} = 1.344787M_{\odot}$ ,  $q = 1.21$ ,  $\tilde{\Lambda} = 172$ ,  $D_L = 40$  Mpc and  $\iota = 45^{\circ}$ . The initial frequency  $f_0$  is 10 Hz. We are showing the differences between the recovered parameters and the injected ones, since the sky position corresponds to the relative best location for each detector. The posterior distributions are comparable, except for the estimation of the declination, where the two-L configuration provides tighter constraints.

relations for the maximum density  $\rho_{\max}^{\text{TOV}}$  and the radius at the maximum mass  $R_{\max}^{\text{TOV}}$ , as described in Sec. II C.

We begin examining the distribution of the maximum density and the radius at the maximum mass, computed from the values of  $f_2$  using the quasi-universal relations (9) and (10), respectively. Figure 9 displays the posterior distributions of  $\Delta\rho_{\max}^{\text{TOV}} = \rho_{\max}^{\text{TOV,PE}} - \rho_{\max}^{\text{TOV}}$  and  $\Delta R_{\max}^{\text{TOV}} = R_{\max}^{\text{TOV,PE}} - R_{\max}^{\text{TOV}}$ , for five different EoSs.  $\rho_{\max}^{\text{TOV}}$  and  $R_{\max}^{\text{TOV}}$  corresponds to the maximal theoretical values obtained from the stable EoS sequence, while  $\rho_{\max}^{\text{TOV,PE}}$  and  $R_{\max}^{\text{TOV,PE}}$  are computed from the fits. We observe that for soft EoSs the distributions of  $\Delta\rho_{\max}^{\text{TOV}}$  are exactly centered around zero, whereas for stiffer EoSs, such as DD2, the distributions are shifted away from zero, although they remain compatible with zero within the 90% CI. This discrepancy arises from the fit relations used in the analysis. In particular examining Fig. 1 of [15], we note that the specific binary with DD2 EoS we used exhibits a larger deviation from the fitted relation for  $\rho_{\max}^{\text{TOV}}$ , although it remains within the 90% CI.

Combining the posteriors of the total mass and the tidal parameters with the results above, we constrain the mass-radius diagram. Figure 10 shows the  $M(R)$  relation for the SLy ( $\mathcal{M} = 1.244295 M_{\odot}$ ) and BLh ( $\mathcal{M} = 1.227164 M_{\odot}$ ) EoSs (See Table II). The con-

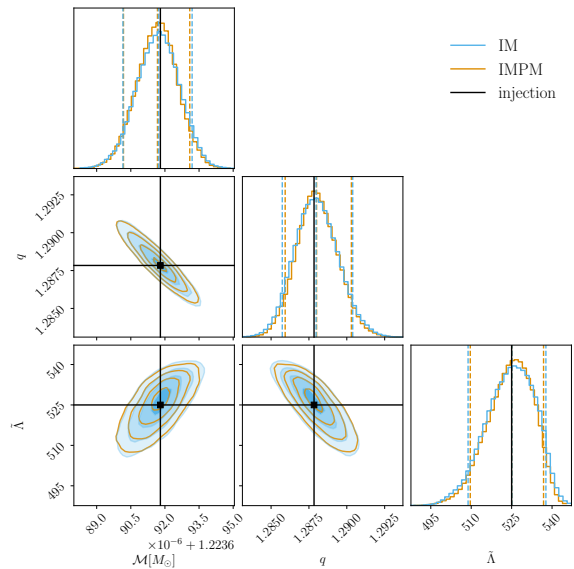


FIG. 7. Posterior distributions for intrinsic parameters recovered from the injection of a BNS using LS220 EoS ( $\mathcal{M} = 1.223692 M_{\odot}$ ), as in Table II. The recovery is performed both with `TEOBResumSPA` (IM) and `TEOBResumSPA_NRPm` (IMPM). The injected values are in black. The posterior distributions obtained with the two models are analogous, since most of the information is included in the IM section.

strained areas are obtained with `TEOBResumSPA` for IM-only and `TEOBResumSPA_NRPm` for IMPM. For PM-only we use the `TEOBResumSPA_NRPm` PE to compute  $R_{\max}^{\text{TOV}}$  and  $\rho_{\max}^{\text{TOV}}$ , but we are not including the constraints on the mass and the tidal polarizability parameter. We utilize the EoSs prior sample of [87] and in our 90% CI 14372 EoSs are included. We additionally test scenarios varying this amount, *i.e.* by doubling it, and obtain consistent results.

The PM gives information at higher densities and together with the IM produces a tighter constraint around the theoretical mass-radius curve, giving in particular a better estimation of the maximum mass  $M_{\max}^{\text{TOV}}$  and the corresponding radius  $R_{\max}^{\text{TOV}}$ . For IMPM, we find the CIs to be  $M_{\max}^{\text{TOV}} = 2.03_{-0.05}^{+0.07} M_{\odot}$  and  $R_{\max}^{\text{TOV}} = 10.23_{-0.12}^{+0.25}$  km for SLy and  $M_{\max}^{\text{TOV}} = 2.07_{-0.08}^{+0.09} M_{\odot}$  and  $R_{\max}^{\text{TOV}} = 10.75_{-0.25}^{+0.32}$  km for BLh. The values we obtain are compatible with [79] and the relative error is roughly the same. Compared with earlier analyses based on GW170817 [86, 100–102], an improvement by a factor three in the uncertainties of the maximum mass is achieved with XG detectors. For  $R_{\max}^{\text{TOV}}$ , the precision enhances by a factor four [103, 104]. We note that in the region of  $1.54M_{\odot} \lesssim M \lesssim 1.87M_{\odot}$ , the constrained IMPM 90% confidence region is not totally consistent with the theoretical mass-radius relation for SLy and BLh. We attribute this slight incompatibility to the sample of EoSs, that does not include EoSs exactly compatible with SLy or BLh at  $M \lesssim 0.6 M_{\odot}$ .

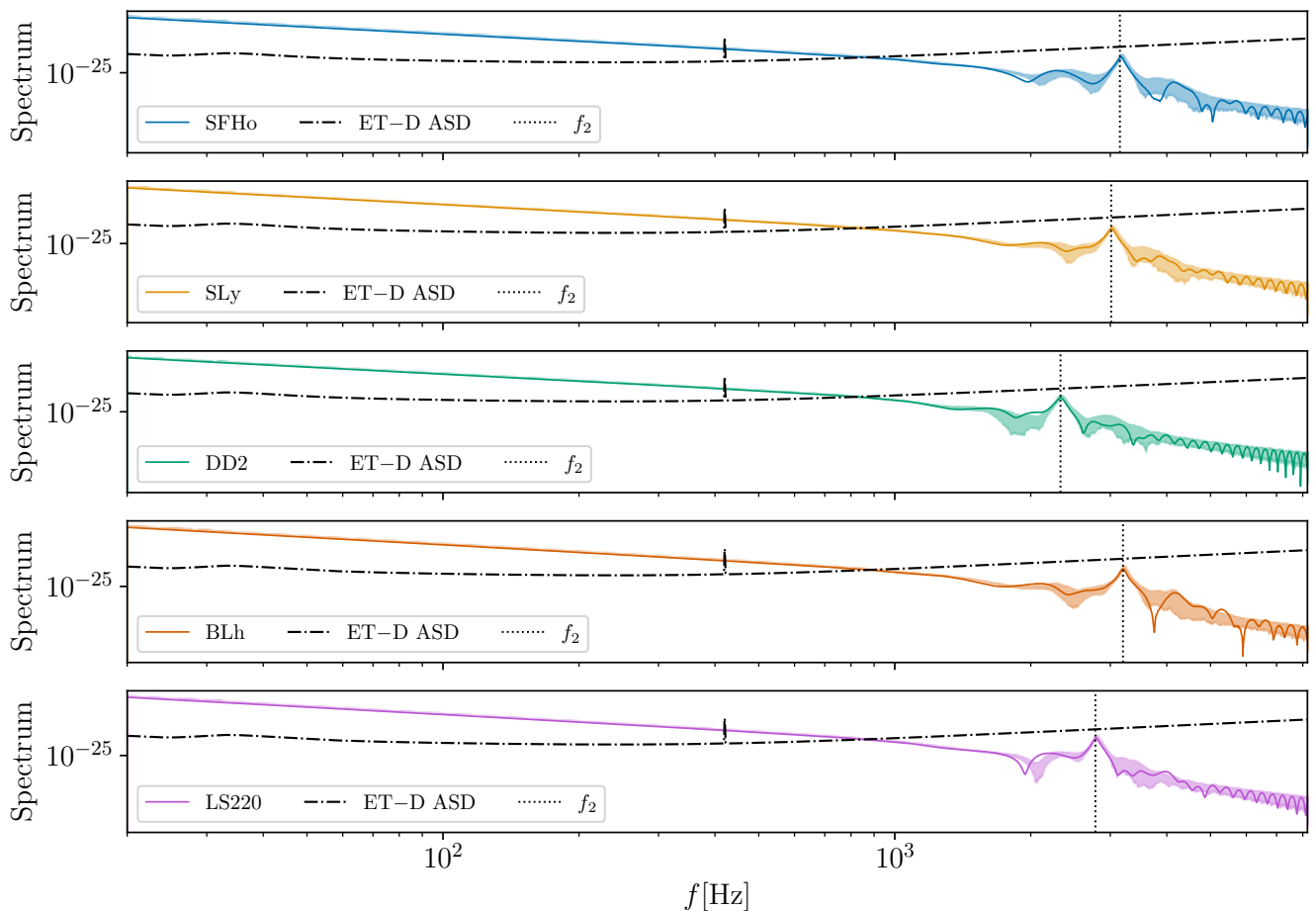


FIG. 8. Injected and recovered spectra of five exemplary binaries, with different EoSs. The solid colored lines report the injected waveforms, the shadowed regions correspond to the 90% credibility regions and the vertical black dotted lines represent the PM peaks at  $f_2$ . We also report the ASD of the ET detector [1, 2]. Both the inspiral part and the peak of the PM are well recovered in all the cases.

Furthermore, Figure 11 reports the  $\Lambda(M)$  curve derived from the combined IMPM analysis, evaluated for an equal-mass binary with BLh EoS,  $M = 2.8M_\odot$  and  $\tilde{\Lambda} = 412$ . The resulting constraint on the tidal polarizability parameter as a function of the mass is particularly tight around the theoretical curve for BLh, highlighting both the accuracy of our method in recovering the theoretical prediction and its robustness in probing the dense matter properties of NSs. From this analysis, we also extract constraints on the tidal polarizability parameter at  $M = 1.4M_\odot$ , finding that it lies within the range  $289 < \Lambda_{1.4} < 529$ .

Finally, Figure 12 displays an example of direct inference of the pressure-density EoS relation. The theoretical SLy curve lies within the 90% CIs for both IM and IMPM cases. We observe a similar behavior to that seen in the mass-radius curve: the confidence region is narrower in the region with  $5 \times 10^{14} \text{ g cm}^{-3} \lesssim \rho \lesssim 13 \times 10^{14} \text{ g cm}^{-3}$ , while it becomes broader at both lower and higher densities. As in the other inferences discussed, the IMPM analysis improves the precision of the inference on  $p(\rho)$

at higher densities.

#### D. Prompt collapse

In this section we discuss the identification of PC. We initially analyze the lower part of Table II, for which we injected GW signals with the IM-only model `TEOBResumSPA`, to simulate a PC. The recovery is performed both with IM and IMPM templates. In these cases the BFs  $\log \mathcal{B}_{\text{IM}}^{\text{IMPM}}$  are negative, with the smallest absolute value reaching  $3.86_{-0.48}^{+0.48}$ . Although these absolute values are smaller than the BFs in the upper part of the Table, there is a strong evidence that the PC hypothesis is favored, because the uncertainties are low enough, implying the pipeline capability of reliably distinguishing PCs. We also note that these BFs are smaller, when comparing with the Bayesian PE of Ref. [13], performed with the time-domain full spectrum `TEOBResumS-NRPM` model. Nevertheless, they remain sufficiently large to robustly confirm the occurrence of a PC.

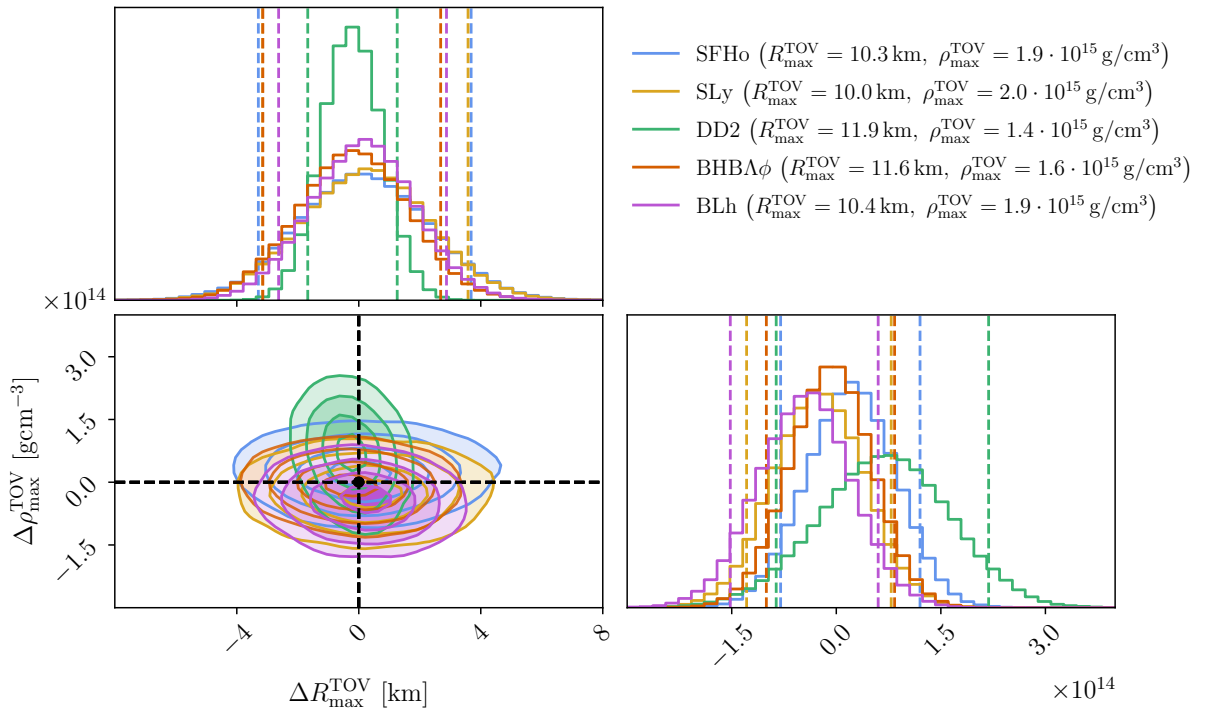


FIG. 9. Posterior distributions of the difference between recovered and theoretical values for maximum density  $\rho_{\max}^{\text{TOV}}$  and radius at the maximum mass  $R_{\max}^{\text{TOV}}$  for five different EoS. The recovered values are computed with Eqs. (9) and (10) and are consistent with the theoretical values from the EoS sequences, as reported in the legend.

While the BF analysis demonstrates that our pipeline can detect PC signatures under favorable conditions, its reliability diminishes as the signal weakens, particularly at larger distances. Notably, for XG detectors, the SNR of the PM typically reaches values on the order of tens, when the binary is located at a distance comparable to that of GW170817 event [78], an exceptionally favorable case. However, the SNR drops below the threshold  $\text{SNR}_{\text{thr}} \sim 7$  (see Paper II) at larger distances. As a result, detecting and characterizing the PM features becomes challenging, and even our pipeline may in principle not be able to reliably distinguish whether there is a PC to a BH or a NS remnant is formed. To address this degeneracy, we consider the alternative methods introduced in Sec. II C to infer PC.

We present in Fig. 13 the probability of PC computed per Eq. (12) for two equal-mass BNSs, assuming SLy EoS ( $M_{\text{thr}} \simeq 2.8 M_{\odot}$ ). The first binary has a total mass  $M = 2.7 M_{\odot} < M_{\text{thr}}$  and the second has  $M = 3.0 M_{\odot} > M_{\text{thr}}$ . In the former case, the probability of PC is approximately 7% for IM-only and 32% for IMPM. This difference comes from the different inferences of the maximum mass and the corresponding radius obtained with IM and IMPM analyses, see Fig. 10. In the IM case  $M_{\max}^{\text{TOV}}$  is on average larger, resulting in a higher threshold mass. In contrast, the IMPM analysis yields a

more precise estimation of the maximum mass, leading to a smaller and more tightly constrained threshold mass.

For the binary with  $M = 3.0 M_{\odot}$ , the probability of PC is 80%, strongly favoring the PC scenario. Therefore, the first system is more likely to result in a long-lived NS remnant, while the second case supports the hypothesis of PC to a BH, as expected from the injection.

In addition, we estimate the values of the time of collapse,  $t_c$ , with `TEOBResumSPA.NRPMw` and we compute the probability of having  $t_c > t_c^{\text{thr}} = 2$  ms. For the first binary ( $M = 2.7 M_{\odot}$ ) we find  $t_c = 23_{-14}^{+15}$  ms, while for the PC injection ( $M = 3.0 M_{\odot}$ ), we find  $t_c = 0.28_{-0.24}^{+0.26}$  ms. From Fig. 13, we notice that the probability  $P(t_c/t_c^{\text{thr}} > X)$  (green region) is vanishing for the latter binary.

Applying the same procedure to real observational data has the potential to place meaningful constraints on the properties of dense matter. Inferring the probability of PC to BH can provide valuable insights into the EoS characterization. This can help identify potential softening of the EoS, which may arise from phase transitions at extreme densities or thermal effects [20, 41, 105–107].

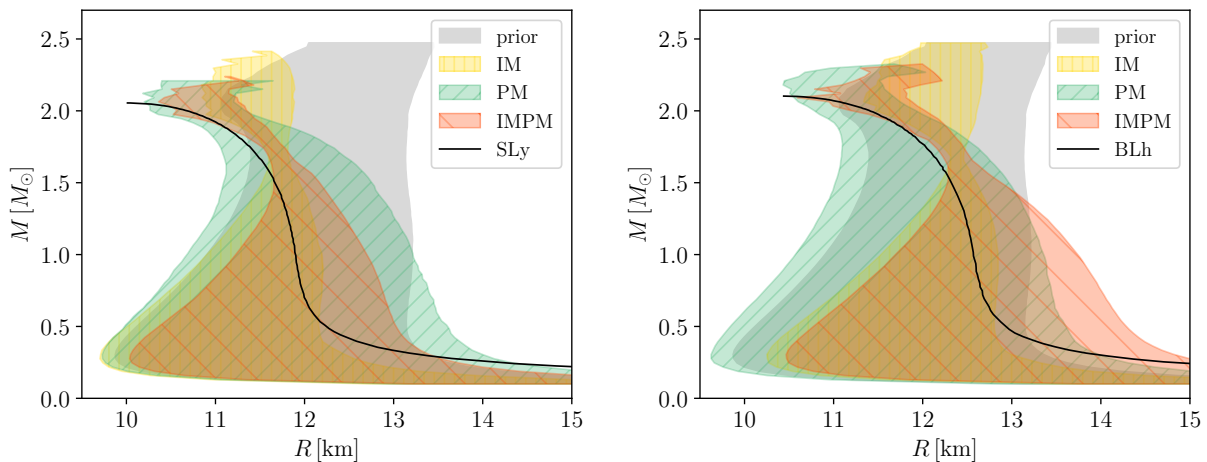


FIG. 10. Mass-radius diagram constraints from two BNS observations, with different EoSs: SLy ( $\mathcal{M} = 1.244295M_{\odot}$ ) on the left and BLh ( $\mathcal{M} = 1.227164M_{\odot}$ ) on the right (See Table II). The gray area (prior) corresponds to the two millions EoS sample of [87]. The colored areas are the 90% credibility regions given by IM, PM and IMPM inferences. The theoretical mass-radius curves are reported in black. The inclusion of the PM gives information in the high-density regime. The further combination with the IM inference leads to tighter constraints of the mass-radius diagram.

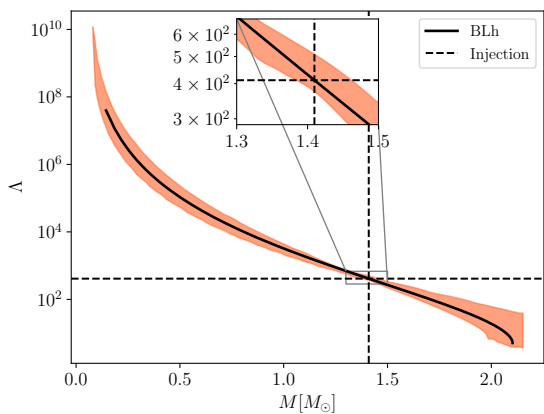


FIG. 11. Tidal polarizability parameter as function of the mass for BLh ( $\mathcal{M} = 1.227164M_{\odot}$ ) EoS (See Table II). The colored region represents the 90% CI for the IMPM inference. It is compatible and tightly constrained around the theoretical  $\Lambda(M)$  curve, shown in black. The dashed lines correspond to the injected values.

#### IV. CONCLUSION

In this paper we presented a waveform model for the complete BNS spectrum and its application to Bayesian parameter estimation with next generation detectors. We focused on single signals in Einstein Telescope's band and the inference of neutron star matter constraints. Methodologically, our work introduces `TEOBResumSPA_NRPm`, a frequency domain waveform model that describes GWs from early inspiral up to kiloHertz PM and considers injection-recovery (mock) Bayesian experiments to vali-

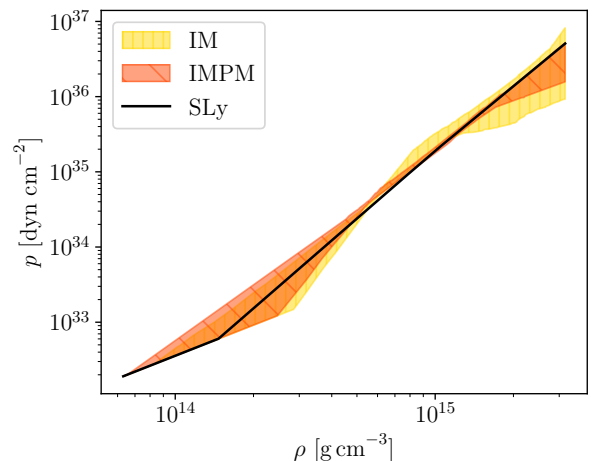


FIG. 12. Pressure-density curve for SLy ( $\mathcal{M} = 1.244295M_{\odot}$ ) EoS (See Table II). The colored regions represent the 90% CIs for the IM (yellow) and IMPM (red) inferences. The theoretical  $p(\rho)$  relation is reported in black. The constrained areas are compatible with the theoretical predictions and the IMPM analysis gives a tighter constraint at higher densities.

date a pipeline that delivers inferences of various extreme matter constraints.

As a preparatory step to full-spectrum analyses, we first considered IM-only injections and study systematically the impact of the choice of the initial frequency (down to 2 Hz), of the signal SNR and the detector configuration on the inference. Notably, we observe an improvement of approximately one order of magnitude in the precision of the chirp mass and mass ratio when lowering the initial frequency from 20 to 2 Hz. The relative

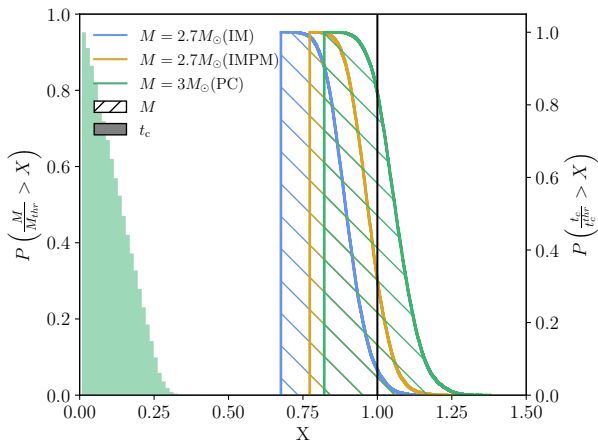


FIG. 13. Cumulative posterior distributions of the ratio between the total mass and the threshold mass for two different binaries. The probability of prompt collapse is represented by the fraction of posterior distribution that lies above the black line. In the case of SLy with  $M = 3 M_{\odot} > M_{\text{thr}}$  the probability of PC is larger than 80%, in the other case ( $M = 2.7 M_{\odot} < M_{\text{thr}}$ ) the probability is smaller than 35%. The difference between IM and IMPM comes from the different ability to constrain the maximum mass, between the two cases, as presented in Sec. III C. The colored area represents the probability distribution for the promptly collapsing binary of having a collapse time larger than the threshold collapse time,  $t_c^{\text{thr}} = 2$  ms. The whole area lies below the black line, therefore the probability is vanishing.

error on reduced tidal parameter improves by about a factor two. Varying the ET configuration from the triangular layout to the two-L configuration does not significantly impact the inference of the intrinsic parameters. Nevertheless, a clear improvement is seen in the measurement of the extrinsic parameters, particularly the declination, which is better constrained with the two-L configuration. This improvement is primarily due to the geographical separation of the two detectors, one in Meuse-Rhine region and the other one in Sardinia, which enhance the ability to localize the source in the sky.

Next, we focused on the full spectrum analysis with the newly developed model `TEOBResumSPA_NRP Mw`. Our pipeline effectively recovers both the injected inspiral segment and the peak frequency of the PM signal. Other PM features are also correctly retrieved, although their constraints are less stringent compared to those on the IM and  $f_2$ . The posterior distributions of chirp mass, mass ratio and reduced tidal parameter, do not show a clear improvement when including the PM spectrum. This is attributed to the PM portion having an SNR approximately two orders of magnitude smaller than that of the IM section. Nevertheless, Bayesian model selection analysis favors the IMPM model over the IM-only, already at postmerger SNR  $\sim 8$  (where the PM detection threshold is 7). This regimes proves to be essential for probing the NS EoSs, as we demonstrate that employing the full

spectrum in the analyses leads to a substantial reduction of the credibility region on the mass-radius diagram, particularly in the high-density regime.

Using an EoS sampling with minimal hypotheses (causality, validity of general relativity), we showed that a single-event PM signal plays a crucial role in constraining both the maximum density and the radius corresponding to the maximum mass, through quasi-universal relations that involves the peak frequency  $f_2$ . The inclusion of these posterior distributions significantly reduces the 90% credibility region of the mass-radius diagram, particularly at high-densities. Therefore, the possibility to perform PEs of GW signals detected with ET, that also contains PM features, enables more precise constraints on the maximum mass and the corresponding radius. In our study, we demonstrate relative errors smaller than 8% and 5% for the maximum mass and the relative neutron star radius, respectively. A novel result presented in this paper is the tight constraint on the  $\Lambda(M)$  curve, where the 90% CI closely follows the theoretical model. Similarly, the inference of the pressure-density relation, especially that obtained through the IMPM analysis, yields significantly tight constraints at high-densities, again closely tracking the theoretical prediction. This approach enhances the precision in extracting information about the properties of nuclear matter under extreme conditions.

Finally, we analyze the inference of prompt collapse scenario. Bayesian model selection with IM-only and IMPM recoveries can identify PC for PM detections at or above the SNR threshold. However, other complementary approaches can be utilized. We extended the approach of Agathos et al. [70] to infer the probability of PC. Our analysis highlights that it is possible to robustly determine whether a BNS undergoes PC or forms a NS remnant that emits PM signals, even if the latter is not detectable due to a weak PM SNR.

Our work has important limitations that should be considered for future work. First, in both IM-only and full spectrum analyses, we injected non-spinning binary systems. In the future, it would be valuable to access the ability of our pipeline to accurately recover spin components, despite the degeneracy between spin, mass ratio and tidal polarizability parameters. An ongoing study is already investigating PE without fixing any parameters in the IMPM scenario. This includes the inference of the spin components as well as additional extrinsic parameters of the binary, beyond just the luminosity distance. Moreover, our current study focuses only on the dominant (2,2) mode. Including also higher-order modes would help, for example to address the degeneracy between luminosity distance and the inclination. `TEOBResumSPA` already incorporates higher modes, whereas their implementation in `NRPMw` is still undergoing. Given that our injections are based on GW signals from XG of detectors, we must also account for the long duration of such signal. In this regime, Earth's rotation is not negligible, and the increased sensitivity of the de-

tector implies that multiple signals may overlap in the data stream. Consequently, future analysis techniques must address challenges in signal disentanglement and noise mitigation [3, 108–110]. Lastly, in our analyses, we used the same model for both injection and recovery. However, Gamba *et al.* [111] showed that for signals with  $\text{SNR} > 80$ , using different waveform models for injection and recovery introduces significant systematic errors. This highlights the importance of waveform systematics studies and motivates the development of more robust cross-model validation strategies.

## ACKNOWLEDGMENTS

The authors thank Nishkal Rao for technical contributions and discussion. GH and SB acknowledge support by the EU Horizon under ERC Consolidator Grant, no. InspiReM-101043372. SB and MB acknowledge support by the EU H2020 under ERC Starting Grant, no. BinGraSp-714626. SB acknowledges support from the Deutsche Forschungsgemeinschaft (DFG) project MEMI (BE 6301/2-1 Projektnummer: 443239082) and GROOVHY (BE 6301/5-1 Projektnummer: 523180871). MB and RG acknowledges support from the Deutsche Forschungsgemeinschaft (DFG) under Grant No. 406116891 within the Research Training Group RTG 2522/1. RG acknowledges support from NSF Grant PHY-2020275 (Network for Neutrinos, Nu-

clear Astrophysics, and Symmetries (N3AS)).

Computations were performed on SuperMUC-NG at the Leibniz-Rechenzentrum (LRZ) Munich and on the national HPE Apollo Hawk at the High Performance Computing Center Stuttgart (HLRS). The authors acknowledge the Gauss Centre for Supercomputing e.V. ([www.gauss-centre.eu](http://www.gauss-centre.eu)) for funding this project by providing computing time on the GCS Supercomputer SuperMUC-NG at LRZ (allocations `pn761i`, `pn36jo` and `pn68wi`). The authors acknowledge HLRS for funding this project by providing access to the supercomputer HPE Apollo Hawk under the grant number IN-TRHYGUE/44215 and MAGNETIST/44288. Postprocessing and development runs were performed on the ARA cluster at Friedrich Schiller University Jena. The ARA cluster is funded in part by DFG grants INST 275/334-1 FUGG and INST 275/363-1 FUGG, and ERC Starting Grant, grant agreement no. BinGraSp-714626.

## V. DATA AVAILABILITY

The waveform model developed in this work, `TEOBResumSPA_NRPm`, is implemented in `bajes` and the software is publicly available at:

<https://github.com/matteobreschi/bajes>

`TEOBResumS` is publicly available at:

<https://bitbucket.org/teobresums/teobresums>.

- 
- [1] S. Hild *et al.*, *Class. Quant. Grav.* **28**, 094013 (2011), arXiv:1012.0908 [gr-qc].
  - [2] S. Hild, *Class. Quant. Grav.* **29**, 124006 (2012), arXiv:1111.6277 [gr-qc].
  - [3] A. Abac *et al.*, (2025), arXiv:2503.12263 [gr-qc].
  - [4] M. Maggiore *et al.* (ET), *JCAP* **03**, 050 (2020), arXiv:1912.02622 [astro-ph.CO].
  - [5] M. Punturo *et al.*, *Class. Quant. Grav.* **27**, 084007 (2010).
  - [6] D. Reitze *et al.*, *Bull. Am. Astron. Soc.* **51**, 035 (2019), arXiv:1907.04833 [astro-ph.IM].
  - [7] M. Evans *et al.*, (2021), arXiv:2109.09882 [astro-ph.IM].
  - [8] E. Belgacem, Y. Dirian, S. Foffa, E. J. Howell, M. Maggiore, and T. Regimbau, *JCAP* **08**, 015 (2019), arXiv:1907.01487 [astro-ph.CO].
  - [9] V. Kalogera *et al.*, (2021), arXiv:2111.06990 [gr-qc].
  - [10] F. Iacovelli, M. Mancarella, S. Foffa, and M. Maggiore, *Astrophys. J.* **941**, 208 (2022), arXiv:2207.02771 [gr-qc].
  - [11] B. P. Abbott *et al.* (LIGO Scientific, Virgo), *Phys. Rev. Lett.* **121**, 161101 (2018), arXiv:1805.11581 [gr-qc].
  - [12] A. Bauswein, O. Just, H.-T. Janka, and N. Stergioulas, *Astrophys. J. Lett.* **850**, L34 (2017), arXiv:1710.06843 [astro-ph.HE].
  - [13] M. Breschi, S. Bernuzzi, F. Zappa, M. Agathos, A. Perego, D. Radice, and A. Nagar, *Phys. Rev. D* **100**, 104029 (2019), arXiv:1908.11418 [gr-qc].
  - [14] D. Radice, S. Bernuzzi, and A. Perego, *Ann. Rev. Nucl. Part. Sci.* **70**, 95 (2020), arXiv:2002.03863 [astro-ph.HE].
  - [15] M. Breschi, S. Bernuzzi, D. Godzieba, A. Perego, and D. Radice, *Phys. Rev. Lett.* **128**, 161102 (2022), arXiv:2110.06957 [gr-qc].
  - [16] M. Wijngaarden, K. Chatziioannou, A. Bauswein, J. A. Clark, and N. J. Cornish, *Phys. Rev. D* **105**, 104019 (2022), arXiv:2202.09382 [gr-qc].
  - [17] B. P. Abbott *et al.* (LIGO Scientific, Virgo), *Phys. Rev. Lett.* **119**, 161101 (2017), arXiv:1710.05832 [gr-qc].
  - [18] B. P. Abbott *et al.* (LIGO Scientific, Virgo, Fermi GBM, INTEGRAL, IceCube, AstroSat Cadmium Zinc Telluride Imager Team, IPN, Insight-Hxmt, ANTARES, Swift, AGILE Team, 1M2H Team, Dark Energy Camera GW-EM, DES, DLT40, GRAWITA, Fermi-LAT, ATCA, ASKAP, Las Cumbres Observatory Group, OzGrav, DWF (Deeper Wider Faster Program), AST3, CAASTRO, VINROUGE, MASTER, J-GEM, GROWTH, JAGWAR, CaltechNRAO, TTU-NRAO, NuSTAR, Pan-STARRS, MAXI Team, TZAC Consortium, KU, Nordic Optical Telescope, ePESSTO, GROND, Texas Tech University, SALT Group, TOROS, BOOTES, MWA, CALET, IKI-GW Follow-up, H.E.S.S., LOFAR, LWA, HAWC, Pierre Auger, ALMA, Euro VLBI Team, Pi of Sky, Chandra Team at McGill University, DFN, ATLAS Telescopes, High Time Resolution Universe Survey, RIMAS, RATIR, SKA South Africa/MeerKAT), *Astrophys. J. Lett.* **848**, L12 (2017), arXiv:1710.05833 [astro-ph.HE].

- [19] B. P. Abbott et al. (LIGO Scientific, Virgo), *Phys. Rev. Lett.* **121**, 161101 (2018), arXiv:1805.11581 [gr-qc].
- [20] D. Radice, S. Bernuzzi, W. Del Pozzo, L. F. Roberts, and C. D. Ott, *Astrophys. J. Lett.* **842**, L10 (2017), arXiv:1612.06429 [astro-ph.HE].
- [21] A. Bauswein, N.-U. F. Bastian, D. B. Blaschke, K. Chatziioannou, J. A. Clark, T. Fischer, and M. Oertel, *Phys. Rev. Lett.* **122**, 061102 (2019), arXiv:1809.01116 [astro-ph.HE].
- [22] E. R. Most and C. A. Raithel, *Phys. Rev. D* **104**, 124012 (2021), arXiv:2107.06804 [astro-ph.HE].
- [23] A. Prakash, D. Radice, D. Logoteta, A. Perego, V. Nedora, I. Bombaci, R. Kashyap, S. Bernuzzi, and A. Endrizzi, *Phys. Rev. D* **104**, 083029 (2021), arXiv:2106.07885 [astro-ph.HE].
- [24] M. Shibata and K. Uryu, *Prog. Theor. Phys.* **107**, 265 (2002), arXiv:gr-qc/0203037.
- [25] N. Stergioulas, A. Bauswein, K. Zagkouris, and H.-T. Janka, *Mon. Not. Roy. Astron. Soc.* **418**, 427 (2011), arXiv:1105.0368 [gr-qc].
- [26] A. Bauswein and H. T. Janka, *Phys. Rev. Lett.* **108**, 011101 (2012), arXiv:1106.1616 [astro-ph.SR].
- [27] A. Bauswein, H. T. Janka, K. Hebeler, and A. Schwenk, *Phys. Rev. D* **86**, 063001 (2012), arXiv:1204.1888 [astro-ph.SR].
- [28] K. Hotokezaka, K. Kiuchi, K. Kyutoku, T. Muranushi, Y.-i. Sekiguchi, M. Shibata, and K. Taniguchi, *Phys. Rev. D* **88**, 044026 (2013), arXiv:1307.5888 [astro-ph.HE].
- [29] K. Takami, L. Rezzolla, and L. Baiotti, *Phys. Rev. Lett.* **113**, 091104 (2014), arXiv:1403.5672 [gr-qc].
- [30] A. Bauswein and N. Stergioulas, *Phys. Rev. D* **91**, 124056 (2015), arXiv:1502.03176 [astro-ph.SR].
- [31] S. Bernuzzi, T. Dietrich, and A. Nagar, *Phys. Rev. Lett.* **115**, 091101 (2015), arXiv:1504.01764 [gr-qc].
- [32] M. Breschi, S. Bernuzzi, K. Chakravarti, A. Camilletti, A. Prakash, and A. Perego, *Phys. Rev. D* **109**, 064009 (2024), arXiv:2205.09112 [gr-qc].
- [33] M. Breschi, R. Gamba, S. Borhanian, G. Carullo, and S. Bernuzzi, (2022), arXiv:2205.09979 [gr-qc].
- [34] A. Puecher, T. Dietrich, K. W. Tsang, C. Kalaghatgi, S. Roy, Y. Setyawati, and C. Van Den Broeck, *Phys. Rev. D* **107**, 124009 (2023), arXiv:2210.09259 [gr-qc].
- [35] A. Bauswein, N. Stergioulas, and H.-T. Janka, *Eur. Phys. J. A* **52**, 56 (2016), arXiv:1508.05493 [astro-ph.HE].
- [36] S. Bose, K. Chakravarti, L. Rezzolla, B. S. Sathyaprakash, and K. Takami, *Phys. Rev. Lett.* **120**, 031102 (2018), arXiv:1705.10850 [gr-qc].
- [37] T. Soultanis, A. Bauswein, and N. Stergioulas, *Phys. Rev. D* **105**, 043020 (2022), arXiv:2111.08353 [astro-ph.HE].
- [38] S. Vretinaris, G. Vretinaris, C. Mermigkas, M. Karamanis, and N. Stergioulas, (2025), arXiv:2501.11518 [gr-qc].
- [39] P. J. Easter, S. Ghonge, P. D. Lasky, A. R. Casey, J. A. Clark, F. H. Vivanco, and K. Chatziioannou, *Phys. Rev. D* **102**, 043011 (2020), arXiv:2006.04396 [astro-ph.HE].
- [40] T. Whittaker, W. E. East, S. R. Green, L. Lehner, and H. Yang, *Phys. Rev. D* **105**, 124021 (2022), arXiv:2201.06461 [gr-qc].
- [41] M. Breschi, G. Carullo, and S. Bernuzzi, *Particles* **6**, 731 (2023), arXiv:2301.09672 [gr-qc].
- [42] L. Rezzolla and K. Takami, *Phys. Rev. D* **93**, 124051 (2016), arXiv:1604.00246 [gr-qc].
- [43] K. Chatziioannou, J. A. Clark, A. Bauswein, M. Millhouse, T. B. Littenberg, and N. Cornish, *Phys. Rev. D* **96**, 124035 (2017), arXiv:1711.00040 [gr-qc].
- [44] L. Lehoucq, I. Dvorkin, and L. Rezzolla, (2025), arXiv:2503.20877 [astro-ph.HE].
- [45] A. Bauswein, N. Stergioulas, and H. T. Janka, *Phys. Rev. D* **90**, 023002 (2014), arXiv:1403.5301 [astro-ph.SR].
- [46] P. J. Easter, P. D. Lasky, A. R. Casey, L. Rezzolla, and K. Takami, *Phys. Rev. D* **100**, 043005 (2019), arXiv:1811.11183 [gr-qc].
- [47] K. Takami, L. Rezzolla, and L. Baiotti, *Phys. Rev. D* **91**, 064001 (2015), arXiv:1412.3240 [gr-qc].
- [48] C. Ecker, T. Gorda, A. Kurkela, and L. Rezzolla, *Nature Commun.* **16**, 1320 (2025), arXiv:2403.03246 [astro-ph.HE].
- [49] J. Bamber, A. Tsokaros, M. Ruiz, and S. L. Shapiro, *Phys. Rev. D* **111**, 044038 (2025), arXiv:2411.00943 [gr-qc].
- [50] S. Mitra, P. Tiwari, and A. Pai, (2025), arXiv:2505.21667 [astro-ph.HE].
- [51] K. Walker, R. Smith, E. Thrane, and D. J. Reardon, *Phys. Rev. D* **110**, 043013 (2024), arXiv:2401.02604 [astro-ph.HE].
- [52] P. K. Gupta, A. Puecher, P. T. H. Pang, J. Janquart, G. Koekoek, and C. Broeck Van Den, (2022), arXiv:2205.01182 [gr-qc].
- [53] F. Iacovelli, M. Mancarella, C. Mondal, A. Puecher, T. Dietrich, F. Gulminelli, M. Maggiore, and M. Oertel, *Phys. Rev. D* **108**, 122006 (2023), arXiv:2308.12378 [gr-qc].
- [54] A. Bandopadhyay, K. Kacanja, R. Somasundaram, A. H. Nitz, and D. A. Brown, *Class. Quant. Grav.* **41**, 225003 (2024), arXiv:2402.05056 [astro-ph.HE].
- [55] R. W. Kiendrebeogo et al., *Astrophys. J.* **958**, 158 (2023), arXiv:2306.09234 [astro-ph.HE].
- [56] A. B. Yelkar, R. O'Shaughnessy, D. Wysocki, and L. Wade, (2024), arXiv:2410.14674 [gr-qc].
- [57] D. A. Coulter et al., *Science* **358**, 1556 (2017), arXiv:1710.05452 [astro-ph.HE].
- [58] R. Chornock et al., *Astrophys. J. Lett.* **848**, L19 (2017), arXiv:1710.05454 [astro-ph.HE].
- [59] M. Nicholl et al., *Astrophys. J. Lett.* **848**, L18 (2017), arXiv:1710.05456 [astro-ph.HE].
- [60] P. S. Cowperthwaite et al., *Astrophys. J. Lett.* **848**, L17 (2017), arXiv:1710.05840 [astro-ph.HE].
- [61] N. R. Tanvir et al., *Astrophys. J. Lett.* **848**, L27 (2017), arXiv:1710.05455 [astro-ph.HE].
- [62] M. Tanaka et al., *Publ. Astron. Soc. Jap.* **69**, psx12 (2017), arXiv:1710.05850 [astro-ph.HE].
- [63] M. Shibata, K. Taniguchi, and K. Uryu, *Phys. Rev. D* **71**, 084021 (2005), arXiv:gr-qc/0503119.
- [64] K. Hotokezaka, K. Kyutoku, H. Okawa, M. Shibata, and K. Kiuchi, *Phys. Rev. D* **83**, 124008 (2011), arXiv:1105.4370 [astro-ph.HE].
- [65] A. Bauswein, T. W. Baumgarte, and H. T. Janka, *Phys. Rev. Lett.* **111**, 131101 (2013), arXiv:1307.5191 [astro-ph.SR].
- [66] R. Kashyap et al., *Phys. Rev. D* **105**, 103022 (2022), arXiv:2111.05183 [astro-ph.HE].
- [67] A. Perego, D. Logoteta, D. Radice, S. Bernuzzi, R. Kashyap, A. Das, S. Padamata, and A. Prakash,

- Phys. Rev. Lett. **129**, 032701 (2022), arXiv:2112.05864 [astro-ph.HE].
- [68] A. Bauswein, S. Blacker, V. Vijayan, N. Stergioulas, K. Chatziioannou, J. A. Clark, N.-U. F. Bastian, D. B. Blaschke, M. Cierniak, and T. Fischer, Phys. Rev. Lett. **125**, 141103 (2020), arXiv:2004.00846 [astro-ph.HE].
- [69] S. D. Tootle, L. J. Papenfort, E. R. Most, and L. Rezzolla, Astrophys. J. Lett. **922**, L19 (2021), arXiv:2109.00940 [gr-qc].
- [70] M. Agathos, F. Zappa, S. Bernuzzi, A. Perego, M. Breschi, and D. Radice, Phys. Rev. D **101**, 044006 (2020), arXiv:1908.05442 [gr-qc].
- [71] B. P. Abbott et al. (LIGO Scientific, Virgo), Astrophys. J. Lett. **892**, L3 (2020), arXiv:2001.01761 [astro-ph.HE].
- [72] S. Akcay, S. Bernuzzi, F. Messina, A. Nagar, N. Ortiz, and P. Rettegno, Phys. Rev. D **99**, 044051 (2019), arXiv:1812.02744 [gr-qc].
- [73] R. Gamba, S. Bernuzzi, and A. Nagar, Phys. Rev. D **104**, 084058 (2021), arXiv:2012.00027 [gr-qc].
- [74] R. Gamba et al., (2023), arXiv:2307.15125 [gr-qc].
- [75] A. Nagar et al., Phys. Rev. D **98**, 104052 (2018), arXiv:1806.01772 [gr-qc].
- [76] A. Nagar, F. Messina, P. Rettegno, D. Bini, T. Damour, A. Geralico, S. Akcay, and S. Bernuzzi, Phys. Rev. D **99**, 044007 (2019), arXiv:1812.07923 [gr-qc].
- [77] A. Nagar and P. Rettegno, Phys. Rev. D **99**, 021501 (2019), arXiv:1805.03891 [gr-qc].
- [78] B. P. Abbott et al. (LIGO Scientific, Virgo), Phys. Rev. X **9**, 031040 (2019), arXiv:1811.12907 [astro-ph.HE].
- [79] M. Breschi, R. Gamba, and S. Bernuzzi, Phys. Rev. D **104**, 042001 (2021), arXiv:2102.00017 [gr-qc].
- [80] J. Veitch et al., Phys. Rev. D **91**, 042003 (2015), arXiv:1409.7215 [gr-qc].
- [81] W. J. Handley, M. P. Hobson, and A. N. Lasenby, Mon. Not. Roy. Astron. Soc. **450**, L61 (2015), arXiv:1502.01856 [astro-ph.CO].
- [82] R. Allison and J. Dunkley, Mon. Not. Roy. Astron. Soc. **437**, 3918 (2014), arXiv:1308.2675 [astro-ph.IM].
- [83] J. S. Speagle, Mon. Not. Roy. Astron. Soc. **493**, 3132 (2020), arXiv:1904.02180 [astro-ph.IM].
- [84] L. Dai, T. Venumadhav, and B. Zackay, (2018), arXiv:1806.08793 [gr-qc].
- [85] B. Zackay, L. Dai, and T. Venumadhav, (2018), arXiv:1806.08792 [astro-ph.IM].
- [86] M. Breschi, R. Gamba, G. Carullo, D. Godzieba, S. Bernuzzi, A. Perego, and D. Radice, Astron. Astrophys. **689**, A51 (2024), arXiv:2401.03750 [astro-ph.HE].
- [87] D. A. Godzieba, D. Radice, and S. Bernuzzi, Astrophys. J. **908**, 122 (2021), arXiv:2007.10999 [astro-ph.HE].
- [88] J. Antoniadis et al., Science **340**, 6131 (2013), arXiv:1304.6875 [astro-ph.HE].
- [89] B. P. Abbott et al. (LIGO Scientific, Virgo), Phys. Rev. X **9**, 011001 (2019), arXiv:1805.11579 [gr-qc].
- [90] D. Foreman-Mackey, D. W. Hogg, D. Lang, and J. Goodman, Publ. Astron. Soc. Pac. **125**, 306 (2013), arXiv:1202.3665 [astro-ph.IM].
- [91] D. Radice, A. Perego, K. Hotokezaka, S. Bernuzzi, S. A. Fromm, and L. F. Roberts, Astrophys. J. Lett. **869**, L35 (2018), arXiv:1809.11163 [astro-ph.HE].
- [92] M. Branchesi et al., JCAP **07**, 068 (2023), arXiv:2303.15923 [gr-qc].
- [93] S. Hild, S. Chelkowski, and A. Freise, (2008), arXiv:0810.0604 [gr-qc].
- [94] M. Punturo et al., Class. Quant. Grav. **27**, 194002 (2010).
- [95] C. Cutler and E. E. Flanagan, Phys. Rev. D **49**, 2658 (1994), arXiv:gr-qc/9402014.
- [96] N. Singh and T. Bulik, Phys. Rev. D **106**, 123014 (2022), arXiv:2107.11198 [astro-ph.HE].
- [97] A. Puecher, A. Samajdar, and T. Dietrich, Phys. Rev. D **108**, 023018 (2023), arXiv:2304.05349 [astro-ph.IM].
- [98] A. Begnoni, S. Anselmi, M. Pieroni, A. Renzi, and A. Ricciardone, (2025), arXiv:2506.21530 [astro-ph.CO].
- [99] J. Skilling, Bayesian Analysis **1**, 833 (2006).
- [100] A. Nathanail, E. R. Most, and L. Rezzolla, Astrophys. J. Lett. **908**, L28 (2021), arXiv:2101.01735 [astro-ph.HE].
- [101] H. Koehn et al., Phys. Rev. X **15**, 021014 (2025), arXiv:2402.04172 [astro-ph.HE].
- [102] R. Essick, I. Tews, P. Landry, S. Reddy, and D. E. Holz, Phys. Rev. C **102**, 055803 (2020), arXiv:2004.07744 [astro-ph.HE].
- [103] N. Rutherford et al., Astrophys. J. Lett. **971**, L19 (2024), arXiv:2407.06790 [astro-ph.HE].
- [104] Y.-Z. Fan, M.-Z. Han, J.-L. Jiang, D.-S. Shao, and S.-P. Tang, Phys. Rev. D **109**, 043052 (2024), arXiv:2309.12644 [astro-ph.HE].
- [105] A. Bauswein, S. Blacker, G. Lioutas, T. Soutanis, V. Vijayan, and N. Stergioulas, Phys. Rev. D **103**, 123004 (2021), arXiv:2010.04461 [astro-ph.HE].
- [106] A. Prakash, I. Gupta, M. Breschi, R. Kashyap, D. Radice, S. Bernuzzi, D. Logoteta, and B. S. Sathyaprakash, Phys. Rev. D **109**, 103008 (2024), arXiv:2310.06025 [gr-qc].
- [107] J. Fields, A. Prakash, M. Breschi, D. Radice, S. Bernuzzi, and A. da Silva Schneider, Astrophys. J. Lett. **952**, L36 (2023), arXiv:2302.11359 [astro-ph.HE].
- [108] F. Cireddu, M. Wils, I. C. F. Wong, P. T. H. Pang, T. G. F. Li, and W. Del Pozzo, Phys. Rev. D **110**, 104060 (2024), arXiv:2312.14614 [gr-qc].
- [109] J. Liu, A. Vajpeyi, R. Meyer, K. Janssens, J. E. Lee, P. Maturana-Russel, N. Christensen, and Y. Liu, Phys. Rev. D **111**, 062003 (2025), arXiv:2409.13224 [gr-qc].
- [110] I. C. F. Wong, P. T. H. Pang, M. Wils, F. Cireddu, W. Del Pozzo, and T. G. F. Li, Phys. Rev. D **111**, 044046 (2025), arXiv:2407.08728 [gr-qc].
- [111] R. Gamba, M. Breschi, S. Bernuzzi, M. Agathos, and A. Nagar, Phys. Rev. D **103**, 124015 (2021), arXiv:2009.08467 [gr-qc].
- [112] S. Bernuzzi, D. Radice, C. D. Ott, L. F. Roberts, P. Moesta, and F. Galeazzi, Phys. Rev. D **94**, 024023 (2016), arXiv:1512.06397 [gr-qc].
- [113] A. Perego, S. Bernuzzi, and D. Radice, Eur. Phys. J. A **55**, 124 (2019), arXiv:1903.07898 [gr-qc].
- [114] S. Bernuzzi et al., Mon. Not. Roy. Astron. Soc. **497**, 1488 (2020), arXiv:2003.06015 [astro-ph.HE].
- [115] S. Bernuzzi, F. Magistrelli, M. Jacobi, D. Logoteta, A. Perego, and D. Radice, (2024), arXiv:2409.18185 [astro-ph.HE].
- [116] A. Gonzalez et al., Class. Quant. Grav. **40**, 085011 (2023), arXiv:2210.16366 [gr-qc].
- [117] G. Riemenschneider, P. Rettegno, M. Breschi, A. Albertini, R. Gamba, S. Bernuzzi, and A. Nagar, Phys. Rev. D **104**, 104045 (2021), arXiv:2104.07533 [gr-qc].
- [118] A. Albertini, A. Nagar, P. Rettegno, S. Albanesi, and R. Gamba, Phys. Rev. D **105**, 084025 (2022), arXiv:2111.14149 [gr-qc].

TABLE III. Summary of the NR simulations used to validate `TEOBResumSPA_NRPm` template. The first column reports the nature of the remnant. The following seven columns show the NR data properties, *i.e.* EoS, reference, total mass  $M$ , mass ratio  $q$ , tidal polarizability  $\kappa_2^T$ , PM peak frequency  $f_2$  and the time of BH collapse  $t_c$ .

Morph.	EOS	Ref.	$M$ [ $M_\odot$ ]	$q$	$\kappa_2^T$	$f_2$ [kHz]	$t_c$ [ms]
Short-lived	SFHo	[112]	2.7	1.0	79	3.42	8.0
	BLQ	[23]	2.8	1.0	81	2.68	2.7
Long-lived	SLy	[13]	2.6	1.0	92	3.13	21
	LS220	[113]	2.6	1.167	168	2.80	35
Tidally disrupted	BLh	[114]	2.84	1.664	97	3.27	18
	DD2	[115]	2.88	1.666	131	2.58	34

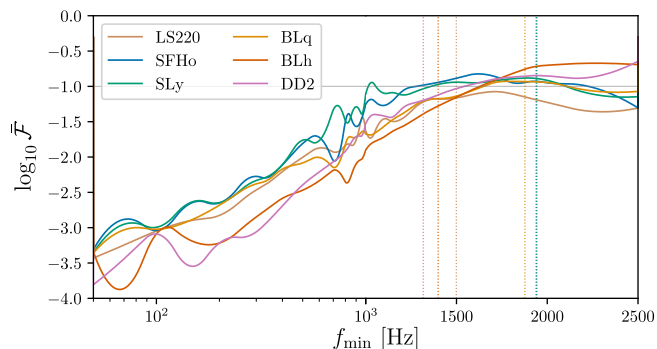


FIG. 14. Unfaithfulness between hybrid NR-EOB waveforms and `TEOBResumSPA_NRPm` model as function of the lower cutoff frequency  $f_{\min}$ . The values are computed employing ET-D [1, 2] sensitivity curve and setting the upper cut-off frequency to 8 kHz. The vertical dotted lines refer to the value of the instantaneous NR frequency at merger for each case.

- [119] B. P. Abbott et al. (LIGO Scientific, Virgo), *Class. Quant. Grav.* **37**, 055002 (2020), arXiv:1908.11170 [gr-qc].
- [120] K. Krishna, A. Vijaykumar, A. Ganguly, C. Talbot, S. Biscoveanu, R. N. George, N. Williams, and A. Zimmerman, (2023), arXiv:2312.06009 [gr-qc].

### Appendix A: Full spectrum model

We provide here some details on the construction and the validation of the complete waveform model `TEOBResumSPA_NRPm` employed in our work.

The complete model is obtained by attaching the EOB `TEOBResumSPA` to `NRPMw` at the merger. Within this framework, the parameters  $\{\phi_{\text{PM}}, t_0\}$  determine the initial phase and time of the PM segment (see Paper I) and are set to the phase and time of merger from the `TEOBResumSPA` waveform,  $\phi_{\text{mrg}}$  and  $t_{\text{mrg}}$ . In order to perform a cleaner attachment and avoid double-counting, when we employ `NRPMw` for the complete IMPM model,

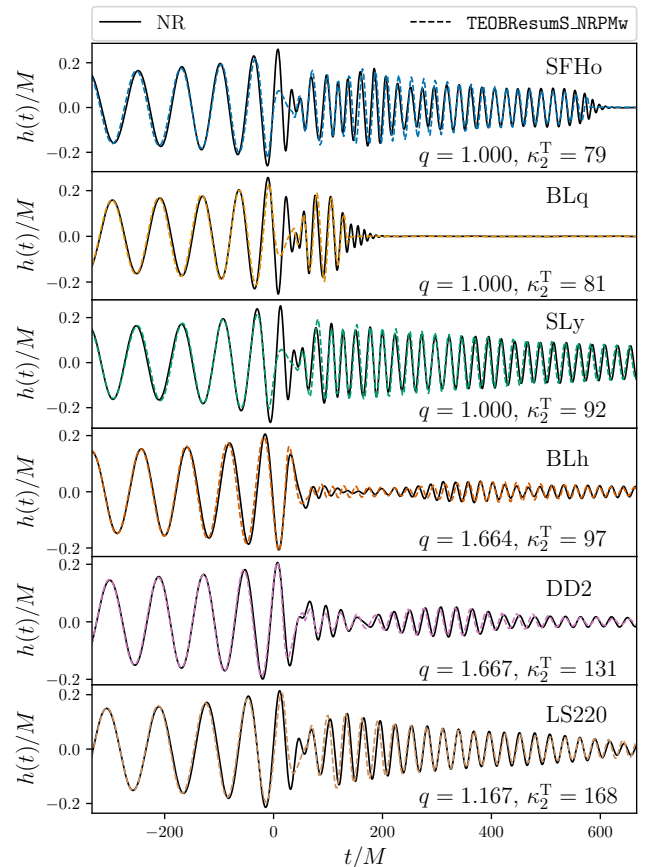


FIG. 15. Comparison between NR data (black solid lines) and `TEOBResumSPA_NRPm` model (colored dashed lines). The reported NR templates correspond to the validation set listed in Tab. III. The time-domain `TEOBResumSPA_NRPm` waveforms are estimated employing inverse FFT. For each NR simulation, we show the corresponding EoS, the mass ratio  $q$  and the tidal polarizability  $\kappa_2^T$ . The waveforms are aligned on the segment  $t/M \leq -200$ .

the fusion wavelet is set to zero, *i.e.*  $W_{\text{fus}} = 0$ , since the EOB model is expected to include the merger portion of data.

The validation of the complete model has been performed using 6 exemplary NR simulations from the CORE database [116] computed with the THC code [23, 66, 112–114] and listed in Tab. III. Note this set of simulations is not included in the calibration set. The data are chosen to cover a sufficiently large variety of phenomenologies; in particular, the validation set includes four long-lived cases, two of which with  $q > 1.5$  showing tidal disruption, and two short-lived cases, one of which includes deconfined quark matter. Moreover, NR data are hybridized with the time-domain `TEOBResumS` model, in order to extended the waveforms in the early-inspiral regime, not included in typical NR simulations. Also for these studies, we employ ET-D sensitivity curve [1, 2] and we minimize over the additional set of param-

ters  $\{\boldsymbol{\theta}_{\text{PM}}^{\text{free}}, \boldsymbol{\delta}_{\text{PM}}\}$  for NRPMw. Employing only the PM portion of data and NRPMw, we obtain  $\log_{10} \bar{\mathcal{F}}$  between  $-1.35$  and  $-0.95$  over all the validation set of 6 binaries. In particular, short-lived cases (SFHo and BLQ) reach  $\log_{10} \bar{\mathcal{F}} \lesssim -1.25$ ; while, large mass ratio binaries (BLh and DD2) recover worst matches, *i.e.*  $\log_{10} \bar{\mathcal{F}} \simeq -0.95$ .

Figure 14 shows the unfaithfulness computed between TEOBResumSPA\_NRPMw model and the hybrid NR-EOB waveforms, where the inner products are evaluated over the frequency range  $[f_{\text{min}}, 8 \text{ kHz}]$ . For  $f_{\text{min}} < 100 \text{ Hz}$ , the model have good agreement with NR data as shown by  $\log_{10} \bar{\mathcal{F}} \lesssim -3$ , comparable to Ref. [73]. Approaching  $f_{\text{mrg}}$ , the recovered  $\bar{\mathcal{F}}$  shows an increasing trend, with peaks above  $10^{-1}$ . Subsequently, for  $f_{\text{min}} > 1.5 \text{ kHz}$ , the recovered  $\bar{\mathcal{F}}$  are comparable with the values obtained only with the PM portion of data, *i.e.*  $\log_{10} \bar{\mathcal{F}} \lesssim -1$ . In order to further inspect this behavior, we show in Fig. 15 the comparison between the time-domain NR data and the corresponding TEOBResumSPA\_NRPMw templates, making use of the inverse FFT. The inspiral EOB template matches NR data accurately up to merger, *i.e.*  $t = 0$ ; however, considerable phase differences arise after this moment in the two models. These errors can be related to the stationary-phase approximation (SPA) and to the absence of next-to-quasi-circular (NQC) corrections [117, 118] in the frequency-domain EOB template. These corrections appear to be more relevant for equal-mass binaries and they motivate additional studies for the development and the calibration of accurate EOB-NR waveform models.

## Appendix B: Mock Bayesian inferences

In this section, we summarize the basic inference techniques implemented in `bajes` pipeline [79]. The main novelty introduced for this work is the implementation of the relative binning technique from [84, 85].

### 1. Bayesian framework

Bayesian analysis is a primary technique to perform parameter estimation. It based on the evaluation of the posterior distribution  $p(\boldsymbol{\theta}|\mathbf{d}, H)$ , through Bayes' theorem,

$$p(\boldsymbol{\theta}|\mathbf{d}, H_S) = \frac{p(\mathbf{d}|\boldsymbol{\theta}, H_S)p(\boldsymbol{\theta}|H_S)}{p(\mathbf{d}|H_S)}, \quad (\text{B1})$$

where the prior distribution  $p(\boldsymbol{\theta}|H_S)$  represents our knowledge about the parameters we estimate,  $p(\mathbf{d}|H_S)$  is the evidence and  $p(\mathbf{d}|\boldsymbol{\theta}, H_S)$  is called likelihood function. For a fixed set of data  $\mathbf{d}(t)$ , the likelihood function is given by

$$\log p(\mathbf{d}|\boldsymbol{\theta}, H_S) \propto -\frac{1}{2} \sum_i (d - h(\boldsymbol{\theta})|d - h(\boldsymbol{\theta}))_i, \quad (\text{B2})$$

where  $H_S$  represents the signal hypothesis, the subscript  $i$  runs over the employed detectors (*i.e.* it denotes that the inner products are estimated with the corresponding data series, projected waveform and PSD for each detector), and the parameter vector  $\boldsymbol{\theta}$  corresponds to the combination  $\boldsymbol{\theta} = \{\boldsymbol{\theta}_{\text{bin}}, \boldsymbol{\theta}_{\text{PM}}^{\text{free}}, \boldsymbol{\delta}_{\text{fit}}, \boldsymbol{\theta}_{\text{ext}}\}$  of the inspiral parameters  $\boldsymbol{\theta}_{\text{bin}}$ , the unconstrained PM parameters  $\boldsymbol{\theta}_{\text{PM}}^{\text{free}}$ , the recalibration coefficients  $\boldsymbol{\delta}_{\text{fit}}$  and the extrinsic GW parameters  $\boldsymbol{\theta}_{\text{ext}} = \{D_L, \iota, \alpha, \delta, \psi, t_{\text{mrg}}, \phi_{\text{mrg}}\}$ . The inner product in Eq. (B2) is

$$(a|b) = \int_{f_0}^{f_{\text{max}}} \frac{a^*(f)b(f)}{S_n(f)} df, \quad (\text{B3})$$

with  $S_n(f)$  the PSD of the noise segment.

Resorting to nested sampling algorithm [99], it is possible to accurately estimate the evidence integral, *i.e.*

$$p(\mathbf{d}|H_S) = \int p(\mathbf{d}|\boldsymbol{\theta}, H_S) p(\boldsymbol{\theta}|H_S) d\boldsymbol{\theta}, \quad (\text{B4})$$

that allows us to perform model selection between two model hypotheses A and B, computing the BF of the signal hypothesis A against the signal hypothesis B as

$$\mathcal{B}_A^B = \frac{p(\mathbf{d}|H_B)}{p(\mathbf{d}|H_A)}. \quad (\text{B5})$$

When  $\mathcal{B}_A^B > 1$  ( $< 1$ ), the model hypothesis B (A) is favored. Furthermore, we introduce the SNR from Eq. (B3) as

$$\rho(h) = \frac{(d_i|h)}{\sqrt{(h|h)}}, \quad (\text{B6})$$

where the definition can be extended to multiple detectors employing quadrature summation.

For a more detailed discussion on the Bayesian framework employed in GW data analysis we remand to [79, 80, 119].

### 2. Relative binning

Relative binning [84, 85, 120] is an acceleration method for PE. The most computationally expensive part of a PE is the evaluation of the likelihood function (B2) with waveforms  $h(f, \boldsymbol{\theta})$  in the parameter space, that are small perturbations of the best-fit waveform. Neighboring waveforms in the frequency domain are very similar to each other, therefore one can work directly with the ratio with respect to a fiducial waveform  $h_0(f)$ ,

$$r(f) = \frac{h(f)}{h_0(f)}. \quad (\text{B7})$$

Since this ratio is smooth, it can be approximated by a piecewise linear function [85]:

$$r(f) = r_0(h, b) + r_1(h, b)(f - f_m(b)), \quad (\text{B8})$$

where  $b$  represents a frequency bin and  $f_m$  is the mean frequency of the bin. Some components of the inner products involved in the likelihood computation can be pre-computed to improve the efficiency:

$$\begin{aligned}
A_0 &= \frac{4}{T} \sum_{f \in b} \frac{d(f)h_0^*(f)}{S_n}, \\
A_1 &= \frac{4}{T} \sum_{f \in b} \frac{d(f)h_0^*(f)}{S_n} (f - f_m(b)), \\
B_0 &= \frac{4}{T} \sum_{f \in b} \frac{|h_0(f)|^2}{S_n}, \\
B_1 &= \frac{4}{T} \sum_{f \in b} \frac{|h_0(f)|^2}{S_n} (f - f_m(b)).
\end{aligned} \tag{B9}$$

Thus, during the PE it is sufficient to evaluate  $r_0(h, b)$  and  $r_1(h, b)$  at the bin edges and compute the inner products for the likelihood as

$$\begin{aligned}
\langle d|h \rangle &= \sum_b (A_0(b)r_0^*(h, b) + A_1(b)r_1^*(h, b)), \\
\langle h|h \rangle &= \sum_b (B_0(b)|r_0(h, b)|^2 + 2B_1(b)\Re[r_0(h, b)r_1^*(h, b)]).
\end{aligned} \tag{B10}$$

We then employ the binning criterion of [85] with  $\epsilon = 0.01$ .

Relative binning technique is effective for waveform analyses up to the merger part, as the frequency domain representations are smooth in this regime. Instead, in the PM regime, the waveform structure becomes highly

complex and rapidly varying in frequency, rendering relative binning inefficient and insufficiently accurate. Nevertheless, `NRPMw` is fast, being phenomenological, therefore acceleration techniques are not critical as in the case of `TEOBResumSPA`. In our full spectrum analyses, we thus employ relative binning only in the IM portion and we perform standard PE for the PM part of the spectrum. To implement this approach, we introduce cutoff frequency  $f_{\text{cut}} = 2048$  Hz. The likelihood is computed separately for the two regimes: using relative binning for frequencies below  $f_{\text{cut}}$  (IM) and using the full, unaccelerated Bayesian PE for frequencies above the cutoff (PM). The total likelihood is obtained by summing the two contributions, cfr. Eq (8). This hybrid approach enables efficient and accurate PE for GW signals spanning both the IM and PM regimes.

The pre-computation of some terms and the evaluation of the waveforms only on the bin edges enable PE of coalescing compact binaries in a very short amount of time: it is possible to run a PE on a single CPU in 44 minutes for a binary black holes, using the `TEOBResumS` template, and in 275 minutes for a BNS with `TaylorF2`. In the case of full spectrum BNSs waveforms with `TEOBResumSPA_NRPMw`, we run on a cluster with 192 CPUs in about 40 hours, making use of the MPI-parallelization of `bajes` [79].

### Appendix C: Results

We report in Table IV the results of the injection-recovery with IM-only `TEOBResumSPA` template relative to Fig. 4 and 5.

TABLE IV: Summary of the PEs with `TEOBResumSPA` for BNSs. The first eight columns report the injected parameters and the last six columns report the recovered values, with the median of the posterior distributions and the 90% credibility regions.

Injected properties								Recovered values											
$\mathcal{M}$ [ $M_\odot$ ]	$q$	$\Lambda$	$\delta\Lambda$	$\chi_{\text{eff}}$	$D_L$ [Mpc]	$f_0$	SNR	$\mathcal{M}$ [ $M_\odot$ ]	$q$	$\Lambda$	$\delta\Lambda$	$\chi_{\text{eff}}$	$D_L$ [Mpc]						
1.3447868	1.212	172	30	0	80	5	2452	1.3447868 <sup>+0.0000005</sup> <sub>-0.0000005</sub>	1.212 <sup>+0.005</sup> <sub>-0.005</sub>	172 <sup>+4</sup> <sub>-6</sub>	40 <sup>+30</sup> <sub>-40</sub>	-0.0000 <sup>+0.0003</sup> <sub>-0.0004</sub>	38.6 <sup>+0.8</sup> <sub>-0.8</sub>						
						10	1775	1.344787 <sup>+0.000003</sup> <sub>-0.000002</sub>	1.21 <sup>+0.02</sup> <sub>-0.01</sub>	171 <sup>+4</sup> <sub>-7</sub>	40 <sup>+30</sup> <sub>-30</sub>	0.0000 <sup>+0.0009</sup> <sub>-0.0007</sub>	38.2 <sup>+1.0</sup> <sub>-0.8</sub>						
						20	1431	1.344788 <sup>+0.000012</sup> <sub>-0.000011</sub>	1.22 <sup>+0.05</sup> <sub>-0.05</sub>	170 <sup>+6</sup> <sub>-12</sub>	30 <sup>+40</sup> <sub>-40</sub>	0.000 <sup>+0.003</sup> <sub>-0.003</sub>	38.2 <sup>+1.2</sup> <sub>-1.1</sub>						
						5	1226	1.3447868 <sup>+0.0000010</sup> <sub>-0.0000009</sub>	1.213 <sup>+0.010</sup> <sub>-0.009</sub>	170 <sup>+6</sup> <sub>-9</sub>	40 <sup>+30</sup> <sub>-50</sub>	0.0001 <sup>+0.0005</sup> <sub>-0.0004</sub>	76 <sup>+2</sup> <sub>-2</sub>						
						10	887	1.344788 <sup>+0.000005</sup> <sub>-0.000004</sub>	1.22 <sup>+0.03</sup> <sub>-0.03</sub>	168 <sup>+7</sup> <sub>-11</sub>	30 <sup>+40</sup> <sub>-50</sub>	0.000 <sup>+0.002</sup> <sub>-0.002</sub>	75 <sup>+3</sup> <sub>-3</sub>						
						20	716	1.34479 <sup>+0.00002</sup> <sub>-0.00002</sub>	1.22 <sup>+0.08</sup> <sub>-0.08</sub>	168 <sup>+7</sup> <sub>-16</sub>	30 <sup>+40</sup> <sub>-50</sub>	0.000 <sup>+0.005</sup> <sub>-0.004</sub>	75 <sup>+3</sup> <sub>-3</sub>						
						5	817	1.344787 <sup>+0.0000014</sup> <sub>-0.0000015</sub>	1.216 <sup>+0.014</sup> <sub>-0.015</sub>	167 <sup>+8</sup> <sub>-13</sub>	30 <sup>+40</sup> <sub>-50</sub>	0.0001 <sup>+0.0008</sup> <sub>-0.0007</sub>	113 <sup>+4</sup> <sub>-4</sub>						
						120	10	592	1.344788 <sup>+0.000007</sup> <sub>-0.000006</sub>	1.22 <sup>+0.04</sup> <sub>-0.04</sub>	166 <sup>+9</sup> <sub>-17</sub>	30 <sup>+40</sup> <sub>-60</sub>	0.000 <sup>+0.002</sup> <sub>-0.002</sub>	113 <sup>+5</sup> <sub>-5</sub>					
						20	477	1.34478 <sup>+0.00004</sup> <sub>-0.00002</sub>	1.19 <sup>+0.14</sup> <sub>-0.13</sub>	168 <sup>+7</sup> <sub>-18</sub>	30 <sup>+40</sup> <sub>-60</sub>	-0.002 <sup>+0.008</sup> <sub>-0.005</sub>	112 <sup>+6</sup> <sub>-6</sub>						
						1.3040200	1.222	192	35	0	80	5	2391	1.3040200 <sup>+0.0000005</sup> <sub>-0.0000005</sub>	1.222 <sup>+0.006</sup> <sub>-0.005</sub>	193 <sup>+4</sup> <sub>-7</sub>	50 <sup>+30</sup> <sub>-40</sub>	-0.0000 <sup>+0.0003</sup> <sub>-0.0003</sub>	38.6 <sup>+0.9</sup> <sub>-0.9</sub>
												10	1731	1.304020 <sup>+0.000002</sup> <sub>-0.000002</sub>	1.22 <sup>+0.02</sup> <sub>-0.02</sub>	192 <sup>+5</sup> <sub>-8</sub>	50 <sup>+30</sup> <sub>-40</sub>	0.0001 <sup>+0.0009</sup> <sub>-0.0008</sub>	38.2 <sup>+1.0</sup> <sub>-0.9</sub>
												20	1396	1.304023 <sup>+0.000009</sup> <sub>-0.000011</sub>	1.24 <sup>+0.04</sup> <sub>-0.05</sub>	190 <sup>+7</sup> <sub>-11</sub>	40 <sup>+40</sup> <sub>-40</sub>	0.001 <sup>+0.003</sup> <sub>-0.003</sub>	38.2 <sup>+1.0</sup> <sub>-1.0</sub>
5	1195	1.3040201 <sup>+0.0000009</sup> <sub>-0.0000009</sub>	1.224 <sup>+0.009</sup> <sub>-0.009</sub>	190 <sup>+6</sup> <sub>-10</sub>	50 <sup>+30</sup> <sub>-40</sub>							0.000 <sup>+0.0005</sup> <sub>-0.0005</sub>	76 <sup>+2</sup> <sub>-2</sub>						
10	865	1.304021 <sup>+0.000004</sup> <sub>-0.000005</sub>	1.23 <sup>+0.03</sup> <sub>-0.03</sub>	189 <sup>+8</sup> <sub>-14</sub>	40 <sup>+40</sup> <sub>-60</sub>							0.000 <sup>+0.002</sup> <sub>-0.002</sub>	76 <sup>+3</sup> <sub>-3</sub>						
20	698	1.30402 <sup>+0.00002</sup> <sub>-0.00002</sub>	1.22 <sup>+0.09</sup> <sub>-0.09</sub>	189 <sup>+9</sup> <sub>-19</sub>	40 <sup>+40</sup> <sub>-60</sub>							-0.000 <sup>+0.006</sup> <sub>-0.004</sub>	75 <sup>+3</sup> <sub>-3</sub>						
5	797	1.3040203 <sup>+0.0000014</sup> <sub>-0.0000013</sub>	1.225 <sup>+0.014</sup> <sub>-0.013</sub>	187 <sup>+9</sup> <sub>-15</sub>	40 <sup>+40</sup> <sub>-60</sub>							0.0002 <sup>+0.0007</sup> <sub>-0.0006</sub>	114 <sup>+5</sup> <sub>-4</sub>						
120	10	577	1.304021 <sup>+0.000006</sup> <sub>-0.000005</sub>	1.23 <sup>+0.04</sup> <sub>-0.04</sub>	186 <sup>+9</sup> <sub>-14</sub>							30 <sup>+40</sup> <sub>-50</sub>	0.000 <sup>+0.002</sup> <sub>-0.002</sub>	114 <sup>+5</sup> <sub>-6</sub>					
20	465	1.30402 <sup>+0.00003</sup> <sub>-0.00002</sub>	1.23 <sup>+0.13</sup> <sub>-0.14</sub>	186 <sup>+10</sup> <sub>-21</sub>	30 <sup>+50</sup> <sub>-60</sub>							0.000 <sup>+0.008</sup> <sub>-0.006</sub>	113 <sup>+6</sup> <sub>-6</sub>						

1.2742305	1.5	232	75	0	80	5	2344	1.2742306 <sup>+0.0000004</sup>	1.500 <sup>+0.003</sup>	233 <sup>+6</sup>	50 <sup>+20</sup>	-0.0001 <sup>+0.0003</sup>	38.5 <sup>+0.9</sup>
						10	1697	1.274232 <sup>+0.0000002</sup>	1.505 <sup>+0.011</sup>	230 <sup>+9</sup>	70 <sup>+30</sup>	0.0001 <sup>+0.0009</sup>	38.1 <sup>+1.2</sup>
						20	1369	1.274231 <sup>+0.0000008</sup>	1.50 <sup>+0.02</sup>	232 <sup>+10</sup>	80 <sup>+20</sup>	0.000 <sup>+0.002</sup>	38.1 <sup>+1.3</sup>
						5	1172	1.2742306 <sup>+0.0000009</sup>	1.501 <sup>+0.006</sup>	231 <sup>+9</sup>	80 <sup>+30</sup>	0.0001 <sup>+0.0006</sup>	76 <sup>+2</sup>
						10	849	1.274231 <sup>+0.0000005</sup>	1.50 <sup>+0.02</sup>	230 <sup>+10</sup>	80 <sup>+30</sup>	0.001 <sup>+0.0025</sup>	75 <sup>+3</sup>
						20	684	1.274230 <sup>+0.0000014</sup>	1.50 <sup>+0.04</sup>	230 <sup>+10</sup>	80 <sup>+30</sup>	0.000 <sup>+0.004</sup>	75 <sup>+3</sup>
1.2037856	1.333	334	75	0	80	5	2238	1.2037856 <sup>+0.0000004</sup>	1.333 <sup>+0.004</sup>	335 <sup>+7</sup>	90 <sup>+40</sup>	0.0000 <sup>+0.0004</sup>	38.5 <sup>+0.8</sup>
						10	1620	1.203786 <sup>+0.0000002</sup>	1.334 <sup>+0.014</sup>	336 <sup>+10</sup>	90 <sup>+50</sup>	-0.0001 <sup>+0.0010</sup>	38.3 <sup>+1.1</sup>
						20	1307	1.203783 <sup>+0.0000011</sup>	1.32 <sup>+0.05</sup>	340 <sup>+10</sup>	90 <sup>+50</sup>	-0.001 <sup>+0.003</sup>	37.9 <sup>+1.3</sup>
						5	1119	1.2037856 <sup>+0.0000008</sup>	1.333 <sup>+0.007</sup>	335 <sup>+10</sup>	100 <sup>+40</sup>	-0.0001 <sup>+0.0006</sup>	76 <sup>+3</sup>
						10	810	1.203786 <sup>+0.0000004</sup>	1.34 <sup>+0.03</sup>	330 <sup>+20</sup>	80 <sup>+60</sup>	0.001 <sup>+0.002</sup>	76 <sup>+3</sup>
						20	654	1.20378 <sup>+0.000002</sup>	1.33 <sup>+0.09</sup>	330 <sup>+10</sup>	90 <sup>+50</sup>	-0.000 <sup>+0.006</sup>	75 <sup>+3</sup>
1.2395655	1.117	385	35	0	80	5	2293	1.2395655 <sup>+0.0000005</sup>	1.117 <sup>+0.009</sup>	385 <sup>+4</sup>	80 <sup>+70</sup>	0.0000 <sup>+0.0002</sup>	38.5 <sup>+0.9</sup>
						10	1660	1.239566 <sup>+0.0000002</sup>	1.12 <sup>+0.02</sup>	385 <sup>+4</sup>	80 <sup>+80</sup>	0.0001 <sup>+0.0007</sup>	38.3 <sup>+1.0</sup>
						20	1339	1.239564 <sup>+0.0000002</sup>	1.10 <sup>+0.02</sup>	385 <sup>+4</sup>	60 <sup>+80</sup>	-0.001 <sup>+0.007</sup>	38.1 <sup>+1.2</sup>
						5	1146	1.2395657 <sup>+0.0000008</sup>	1.121 <sup>+0.015</sup>	381 <sup>+7</sup>	50 <sup>+90</sup>	0.0001 <sup>+0.0005</sup>	76 <sup>+3</sup>
						10	830	1.239566 <sup>+0.0000004</sup>	1.12 <sup>+0.05</sup>	382 <sup>+7</sup>	50 <sup>+90</sup>	0.000 <sup>+0.002</sup>	76 <sup>+3</sup>
						20	670	1.239566 <sup>+0.0000018</sup>	1.13 <sup>+0.11</sup>	380 <sup>+9</sup>	30 <sup>+110</sup>	0.000 <sup>+0.005</sup>	75 <sup>+3</sup>
1.3153039	1.289	442	75	0	80	5	764	1.2395657 <sup>+0.0000012</sup>	1.12 <sup>+0.02</sup>	380 <sup>+9</sup>	50 <sup>+100</sup>	0.0001 <sup>+0.0007</sup>	113 <sup>+5</sup>
						10	553	1.239566 <sup>+0.0000006</sup>	1.13 <sup>+0.06</sup>	380 <sup>+10</sup>	40 <sup>+100</sup>	0.000 <sup>+0.006</sup>	112 <sup>+5</sup>
						20	446	1.23956 <sup>+0.000005</sup>	1.13 <sup>+0.08</sup>	380 <sup>+10</sup>	40 <sup>+120</sup>	0.000 <sup>+0.002</sup>	112 <sup>+5</sup>
						5	2407	1.3153038 <sup>+0.0000005</sup>	1.289 <sup>+0.005</sup>	444 <sup>+9</sup>	100 <sup>+70</sup>	0.0000 <sup>+0.0003</sup>	38.5 <sup>+0.9</sup>
						10	1742	1.315303 <sup>+0.0000003</sup>	1.28 <sup>+0.02</sup>	449 <sup>+10</sup>	120 <sup>+70</sup>	-0.0004 <sup>+0.0011</sup>	38.2 <sup>+1.1</sup>
						20	1405	1.315296 <sup>+0.0000017</sup>	1.26 <sup>+0.07</sup>	452 <sup>+9</sup>	120 <sup>+70</sup>	-0.002 <sup>+0.004</sup>	38.0 <sup>+1.1</sup>
1.2236919	1.288	526	110	0	80	5	1204	1.3153039 <sup>+0.0000010</sup>	1.290 <sup>+0.009</sup>	444 <sup>+13</sup>	100 <sup>+80</sup>	-0.0001 <sup>+0.0005</sup>	76 <sup>+3</sup>
						10	871	1.315303 <sup>+0.0000010</sup>	1.29 <sup>+0.03</sup>	450 <sup>+10</sup>	13 <sup>+70</sup>	-0.000 <sup>+0.006</sup>	75 <sup>+3</sup>
						20	702	1.315300 <sup>+0.0000024</sup>	1.27 <sup>+0.10</sup>	450 <sup>+10</sup>	110 <sup>+80</sup>	-0.001 <sup>+0.006</sup>	75 <sup>+4</sup>
						5	802	1.3153038 <sup>+0.0000016</sup>	1.29 <sup>+0.01</sup>	440 <sup>+10</sup>	120 <sup>+70</sup>	-0.0000 <sup>+0.0008</sup>	114 <sup>+5</sup>
						10	581	1.315306 <sup>+0.0000006</sup>	1.30 <sup>+0.04</sup>	440 <sup>+20</sup>	90 <sup>+90</sup>	0.001 <sup>+0.002</sup>	112 <sup>+1</sup>
						20	468	1.31530 <sup>+0.000003</sup>	1.27 <sup>+0.11</sup>	445 <sup>+15</sup>	110 <sup>+80</sup>	-0.001 <sup>+0.008</sup>	112 <sup>+6</sup>
1.1076460	1.125	570	50	0	80	5	2268	1.2236917 <sup>+0.0000005</sup>	1.286 <sup>+0.005</sup>	530 <sup>+9</sup>	150 <sup>+70</sup>	-0.0000 <sup>+0.0004</sup>	38.6 <sup>+1.0</sup>
						10	1642	1.223691 <sup>+0.0000003</sup>	1.28 <sup>+0.02</sup>	535 <sup>+11</sup>	190 <sup>+40</sup>	-0.0005 <sup>+0.0012</sup>	38.2 <sup>+1.2</sup>
						20	1325	1.223690 <sup>+0.0000003</sup>	1.28 <sup>+0.02</sup>	533 <sup>+9</sup>	160 <sup>+80</sup>	-0.001 <sup>+0.003</sup>	38.1 <sup>+1.3</sup>
						5	1134	1.2236918 <sup>+0.0000009</sup>	1.287 <sup>+0.009</sup>	529 <sup>+11</sup>	160 <sup>+60</sup>	-0.0000 <sup>+0.0006</sup>	76 <sup>+2</sup>
						10	821	1.223692 <sup>+0.0000004</sup>	1.29 <sup>+0.03</sup>	529 <sup>+13</sup>	170 <sup>+60</sup>	-0.000 <sup>+0.002</sup>	75 <sup>+3</sup>
						20	662	1.22369 <sup>+0.000004</sup>	1.30 <sup>+0.09</sup>	522 <sup>+18</sup>	130 <sup>+90</sup>	0.001 <sup>+0.006</sup>	75 <sup>+3</sup>
1.1076460	1.125	570	50	0	120	5	756	1.2236919 <sup>+0.0000014</sup>	1.289 <sup>+0.014</sup>	525 <sup>+14</sup>	160 <sup>+100</sup>	0.0001 <sup>+0.007</sup>	113 <sup>+5</sup>
						10	547	1.223694 <sup>+0.0000006</sup>	1.30 <sup>+0.04</sup>	520 <sup>+20</sup>	140 <sup>+90</sup>	0.001 <sup>+0.003</sup>	112 <sup>+6</sup>
						20	442	1.22369 <sup>+0.000007</sup>	1.29 <sup>+0.12</sup>	523 <sup>+18</sup>	140 <sup>+120</sup>	0.000 <sup>+0.003</sup>	112 <sup>+5</sup>
						5	2089	1.1076460 <sup>+0.0000004</sup>	1.125 <sup>+0.008</sup>	570 <sup>+6</sup>	90 <sup>+140</sup>	0.0000 <sup>+0.0003</sup>	38.4 <sup>+0.8</sup>
						10	1514	1.107646 <sup>+0.0000002</sup>	1.13 <sup>+0.03</sup>	569 <sup>+6</sup>	60 <sup>+100</sup>	0.0002 <sup>+0.0008</sup>	38.2 <sup>+1.4</sup>
						20	1222	1.107646 <sup>+0.0000008</sup>	1.13 <sup>+0.07</sup>	567 <sup>+7</sup>	50 <sup>+120</sup>	0.000 <sup>+0.003</sup>	38.0 <sup>+1.3</sup>
1.1076460	1.125	570	50	0	120	5	1045	1.1076460 <sup>+0.0000007</sup>	1.126 <sup>+0.014</sup>	567 <sup>+8</sup>	140 <sup>+90</sup>	0.0001 <sup>+0.0005</sup>	76 <sup>+2</sup>
						10	757	1.107647 <sup>+0.0000003</sup>	1.13 <sup>+0.04</sup>	568 <sup>+9</sup>	80 <sup>+160</sup>	0.0003 <sup>+0.0016</sup>	76 <sup>+3</sup>
						20	611	1.107646 <sup>+0.0000017</sup>	1.14 <sup>+0.12</sup>	565 <sup>+10</sup>	70 <sup>+150</sup>	0.000 <sup>+0.010</sup>	75 <sup>+3</sup>
						5	696	1.1076461 <sup>+0.0000011</sup>	1.13 <sup>+0.02</sup>	564 <sup>+11</sup>	90 <sup>+130</sup>	0.0001 <sup>+0.0006</sup>	113 <sup>+5</sup>
						10	505	1.107646 <sup>+0.0000005</sup>	1.13 <sup>+0.06</sup>	565 <sup>+11</sup>	90 <sup>+220</sup>	0.000 <sup>+0.006</sup>	113 <sup>+5</sup>
						20	407	1.107643 <sup>+0.0000019</sup>	1.11 <sup>+0.14</sup>	560 <sup>+13</sup>	90 <sup>+190</sup>	-0.001 <sup>+0.007</sup>	112 <sup>+6</sup>